nature neuroscience

ARTICLES

https://doi.org/10.1038/s41593-022-01060-2

Check for updates

Cerebrospinal fluid can exit into the skull bone marrow and instruct cranial hematopoiesis in mice with bacterial meningitis

Fadi E. Pulous[1,2,12], Jean C. Cruz-Hernández[1,3,12], Chongbo Yang[1,2], Zeynep Kaya[1,2], Alexandre Paccalet[1,2], Gregory Wojtkiewicz[1], Diane Capen[4], Dennis Brown[4], Juwell W. Wu[1,3], Maximilian J. Schloss[1,2], Claudio Vinegoni[1,2], Dmitry Richter[1,3], Masahiro Yamazoe[1,2], Maarten Hulsmans[1,2], Noor Momin[1,2], Jana Grune[1,2], David Rohde[1,2], Cameron S. McAlpine[5,6], Peter Panizzi[7], Ralph Weissleder[1,2], Dong-Eog Kim[8], Filip K. Swirski[5], Charles P. Lin[1,3,13] ✉, Michael A. Moskowitz[1,2,9,13] ✉ and Matthias Nahrendorf[1,2,10,11,13] ✉

Interactions between the immune and central nervous systems strongly influence brain health. Although the blood–brain barrier restricts this crosstalk, we now know that meningeal gateways through brain border tissues facilitate intersystem communication. Cerebrospinal fluid (CSF), which interfaces with the glymphatic system and thereby drains the brain's interstitial and perivascular spaces, facilitates outward signaling beyond the blood–brain barrier. In the present study, we report that CSF can exit into the skull bone marrow. Fluorescent tracers injected into the cisterna magna of mice migrate along perivascular spaces of dural blood vessels and then travel through hundreds of sub-millimeter skull channels into the calvarial marrow. During meningitis, bacteria hijack this route to invade the skull's hematopoietic niches and initiate cranial hematopoiesis ahead of remote tibial sites. As skull channels also directly provide leukocytes to meninges, the privileged sampling of brain-derived danger signals in CSF by regional marrow may have broad implications for inflammatory neurological disorders.

In addition to guarding brain health, the immune system participates in a wide array of neurological disorders. The blood–brain barrier enforces an unusually rigid leukocyte origin dichotomy, dividing central nervous system (CNS)-resident immune cells from systemically circulating leukocytes[1]. Crosstalk between local brain and systemic immune system components is limited in the steady state, but expands during pathologies[2–4]. Residing at potential portals of entry, the meninges are CNS border tissues that provide the brain and spinal cord with a protective connective tissue capsule consisting of three layers (pia mater, arachnoid and dura mater) within which CSF flows between the arachnoidal membrane and pia mater[5]. Ultimately, CSF exits into the venous blood and the lymphatics[6,7].

The CNS border tissues dynamically police leukocyte migration and brain-derived signal exit. Recently discovered skull channels connecting the cranial bone marrow to the meninges, in mice and humans, constitute a novel leukocyte portal into the CNS[8–11]. Skull hematopoietic activity directly adjacent to the brain delivers myeloid cells[8,11] and lymphocytes[10], bypassing the blood–brain barrier. Clinical data indicate that meningeal leukocyte populations correlate closely with those found in neighboring brain lesions[12]. Given that the skull marrow is a private leukocyte purveyor for the brain, skull-derived immune cells may be an intermediate third entity between resident and nonresident CNS leukocytes. Furthermore, dural lymphatics provide a CSF outflow that freely exchanges with the brain's glymphatic system[13]. This signaling pathway shares information about brain health systemically, allowing for presentation of CNS-derived antigen in cervical lymph nodes and consequently activating adaptive immunity[14,15]. Collectively, these reports expand our understanding of immune cell function across CNS borders and specifically implicate CSF as an under-appreciated messenger that may coordinate neuroinflammation.

In the present study, we describe previously unrecognized CSF outflow that permeates the skull bone marrow. Fluorescent tracers injected into the cisterna magna of mice migrate along the perivascular spaces of dural blood vessels and then perivascularly travel through skull channels into the cranial marrow. In mice with meningitis, bacteria usurp this path into the skull marrow, thereby boosting cranial emergency hematopoiesis.

[1]Center for Systems Biology, Massachusetts General Hospital and Harvard Medical School, Boston, MA, USA. [2]Department of Radiology, Massachusetts General Hospital and Harvard Medical School, Boston, MA, USA. [3]Wellman Center for Photomedicine, Massachusetts General Hospital and Harvard Medical School, Boston, MA, USA. [4]Program in Membrane Biology, Division of Nephrology, Department of Medicine, Harvard Medical School and Massachusetts General Hospital, Boston, MA, USA. [5]Cardiovascular Research Institute and Department of Medicine, Icahn School of Medicine at Mount Sinai, New York, NY, USA. [6]Nash Family Department of Neuroscience, Icahn School of Medicine at Mount Sinai, New York, NY, USA. [7]Department of Drug Discovery and Development, Harrison School of Pharmacy, Auburn University, Auburn, AL, USA. [8]Molecular Imaging and Neurovascular Research Laboratory, Department of Neurology, Dongguk University College of Medicine, Goyang, South Korea. [9]Department of Neurology, Massachusetts General Hospital and Harvard Medical School, Boston, MA, USA. [10]Cardiovascular Research Center, Massachusetts General Hospital and Harvard Medical School, Boston, MA, USA. [11]Department of Internal Medicine I, University Hospital Wuerzburg, Wuerzburg, Germany. [12]These authors contributed equally: Fadi E. Pulous, Jean C. Cruz-Hernández. [13]These authors jointly supervised this work: Charles P. Lin, Michael A. Moskowitz, Matthias Nahrendorf. ✉e-mail: charles_lin@hms.harvard.edu; moskowitz@helix.mgh.harvard.edu; mnahrendorf@mgh.harvard.edu

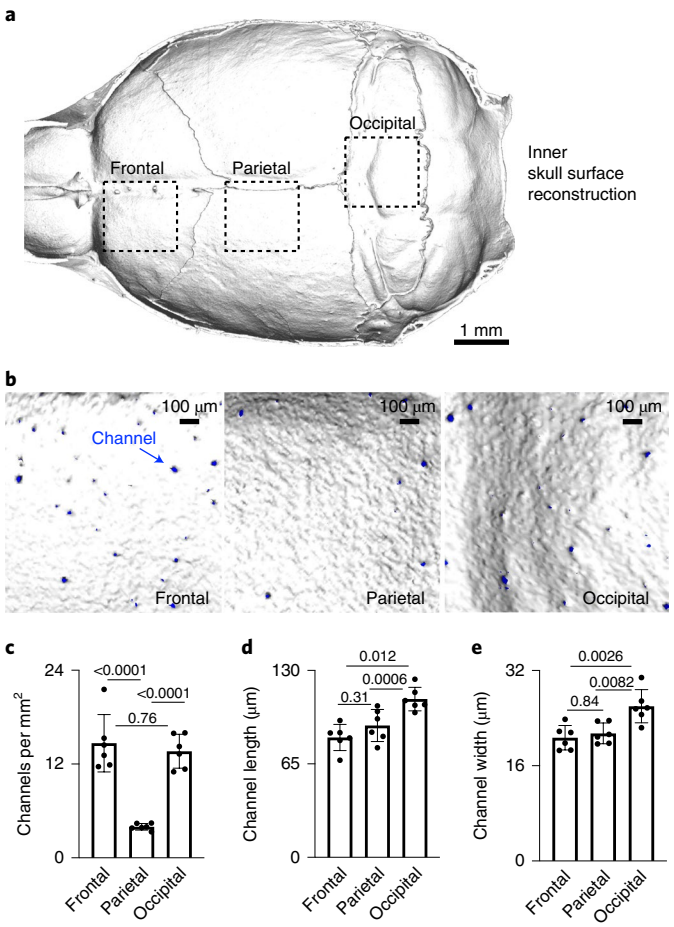

Fig. 1 | Skull channel anatomy by X-ray CT. a, Inner skull cortex micro-CT surface reconstruction. **b**, Reconstruction of inner frontal, parietal and occipital bone surfaces. Channel openings are labeled blue. There are two independent repeats. **c**–**e**, Channel density (**c**), length (**d**) and width (**e**) (mean ± s.d., $n = 6$; *P* values represent a one-way ANOVA with Tukey's multiple comparison test).

Results

Perivascular CSF transits through skull channels into marrow cavities. To understand the spatial organization of the skull channels, we first performed high-resolution, ex vivo X-ray computed tomography (CT) of the skull (Fig. 1a) and characterized regional channel networks overlying frontal, parietal and occipital brain lobes (Fig. 1b). Channels traversed the inner compact bone into the marrow-containing cavities. We observed the highest density of skull channels in the frontal and occipital regions (Fig. 1c). Given a CT-derived mean channel density >10 per mm^2 and an inner skull surface area >100 mm^2, we estimate that >1,000 channels reach into the cranial vault of an adult mouse. Frontal and parietal skull channels formed the shortest connections to the dura, ranging from 83 µm to 90 µm, whereas occipital skull channels were approximately 25% longer (Fig. 1d). Frontal and parietal skull channels were 20% narrower than their occipital counterparts (Fig. 1e), pointing to regional channel heterogeneity.

We hypothesized that these numerous links between the skull marrow and the dura enable not only cell traffic toward the meninges[8] but also bidirectional crosstalk. We therefore implemented a two-photon intravital microscopy (IVM) and an ex vivo imaging pipeline to visualize CSF distribution after fluorescent tracer injection into the cisterna magna[16,17]. Intracisternal injection of FITC-labeled ovalbumin was combined with intravenous labeling of the blood pool using Texas Red-labeled Dextran. We observed a striking perivascular appearance of the intracisternal tracer along a subset of dural vessels (Fig. 2a and Supplementary Video 1), indicating that CSF travels perivascularly from the subarachnoid space into the dura. This led us to wonder whether we could track this CSF outflow into the skull marrow cavity. We labeled cranial vasculature with intravenously injected, fluorescently conjugated CD31/Sca1 antibodies and CSF with intracisternally (IC) injected, fluorescently labeled ovalbumin, followed by intravital imaging of the skull marrow cavity[8,18,19]. In the skull marrow, we detected perivascular spaces and cells labeled with the IC injected CSF tracer (Fig. 2b). This critical observation in the dura and marrow suggested that perivascular CSF flow into the marrow may occur through skull channels.

As we anticipated, high-magnification transmission electron microscopy (TEM) analysis of skull channels revealed a perivascular space that may accommodate CSF transport beginning at the dural channel opening (Fig. 2c). To directly test this hypothesis, we labeled cranial vasculature with intravenous Texas Red Dextran and the CSF with an intracisternal FITC–Dextran injection 1 h before ex vivo microscopy of the inner skull cortex. Channel cross-sections were clearly demarcated by dextran-labeled vessels surrounded by bone visualized with second harmonic generation (Fig. 2d). The *z*-stacks that began on the dural surface and moved deep into the marrow cavity visualized IC injected dextran in numerous skull channels (Fig. 2d and Supplementary Video 2). This signal surrounded the blood vessel and was present from channels' dural openings all the way into the marrow cavity. Counting CSF-tracer-containing channels revealed that 67% of them showed perivascular signal after intracisternal dextran injection (Fig. 2e,f). In frontal, parietal and occipital bone, most skull channels exhibited perivascular signal after intracisternal tracer injection (Extended Data Fig. 1). It remains to be determined whether all skull channels can accommodate CSF flow, and whether there are functional or anatomical reasons for the observed heterogeneity, for example, the direction of blood flow through the channel's vessel or absence of a perivascular space.

Bone marrow imaging after intracisternal injection revealed a similar perivascular appearance for tracers with molecular masses from 66 kDa to 2,000 kDa along a subset of skull marrow vessels (Fig. 2g). Labeled CSF was detected in the skull marrow as early as 15–30 min after injection but was largely absent from the tibia's marrow vasculature (Fig. 2b and Extended Data Fig. 2); this indicates that CSF was excluded from systemic circulation at early timepoints. Together, these data demonstrate that CSF can exit the subarachnoid space via perivascular flux along a subset of dural vessels that connect into the bone marrow cavity through an extensive skull channel network. This finding implicates the skull marrow as a CSF-sensing hematopoietic compartment. We next sought to examine these observations' relevance in a mouse model of acute CNS inflammation, bacterial meningitis.

***S. pneumoniae* expand near dural skull channel openings.** We adapted a model of pneumococcal meningitis[20] to test the functional significance of skull channel connections in neuroinflammation. *S. pneumoniae* is the clinically dominant cause of bacterial meningitis[21]. To establish a disease timeline in mice, we injected 5×10^3 bioluminescent *S. pneumoniae* Xen10 bacteria into the cisterna magna and analyzed bacterial propagation over time, alongside control mice that received an equal volume of artificial CSF (aCSF; Fig. 3a). Whole-body bioluminescence (BLI) imaging revealed a time-dependent signal increase reporting bacterial growth (Fig. 3b). The BLI signal was observed predominantly in the skull 36 h after injection and by 48 h had spread to the spine. Bacterial burden increased exponentially by 36 h, with a peak at 48 h after injection (Fig. 3c). To assess meningeal inflammation, we measured the canonical inflammatory cytokines *Il1β*, *Il6* and *TNFα* in

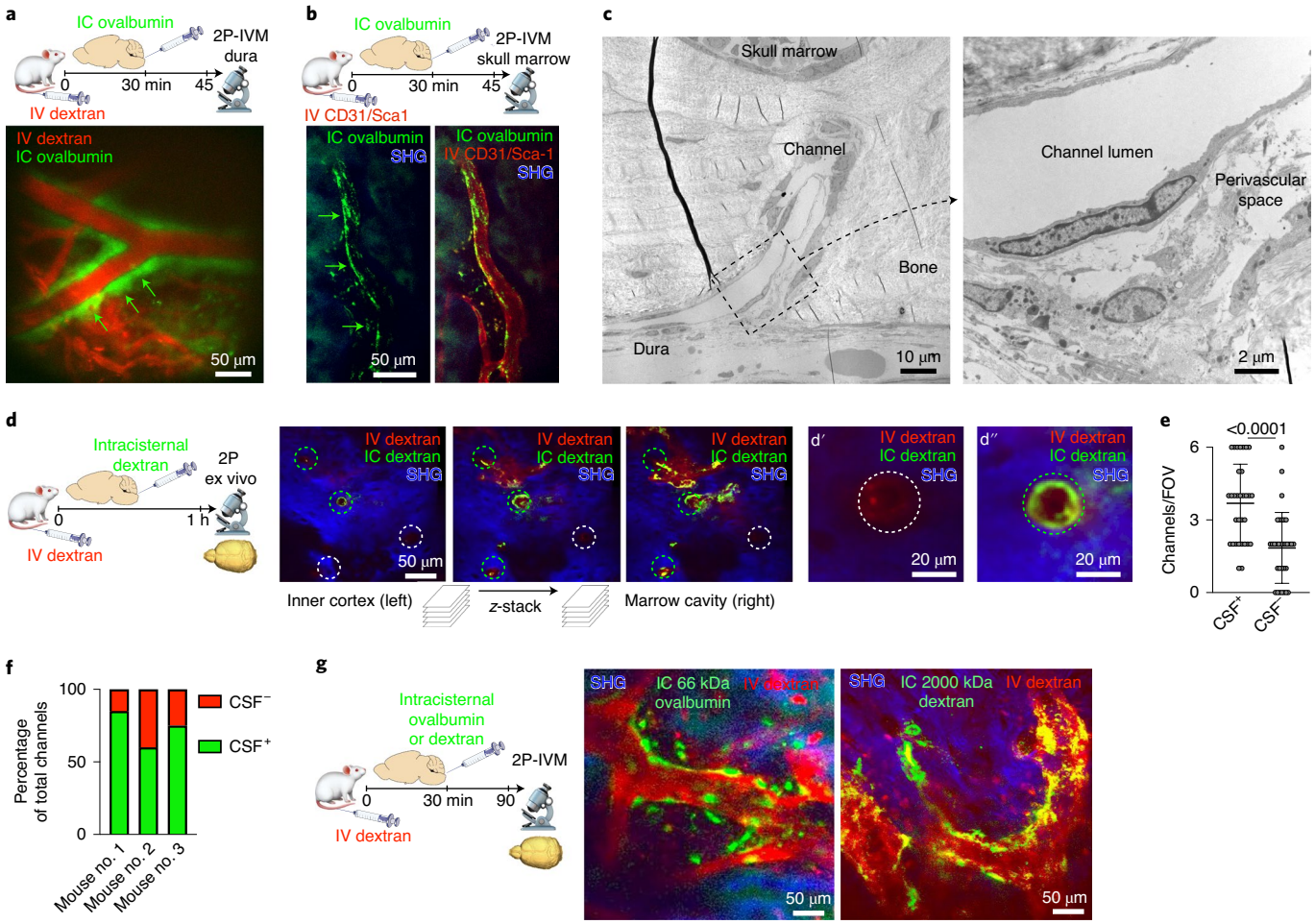

Fig. 2 | CSF flows through the perivascular space of skull channels into the marrow. a, Two-photon (2P) IVM image of IC injected ovalbumin in the perivascular space of a dural vessel labeled with intravenous (IV) dextran ($n=3$ from 2 experiments). **b**, IVM of IC injected ovalbumin in the perivascular space of a marrow vessel ($n=3$ from 2 experiments). **c**, TEM of skull channel. Inset shows perivascular spaced ($n=6$ from 2 experiments). **d**, Ex vivo *z*-stack (54-µm stack at 1 µm per step) of interior frontal and parietal skull cortex after intracisternal and intravenous dextran. Bone is visualized by second harmonic generation around channels (circles). The d′ and d′′ depict intracisternal tracer-negative and -positive channels ($n=3$ from 2 experiments). **e**, Number of CSF-containing channels (mean ± s.d.; $n=3$; *P* value represents Mann–Whitney, two-sided rank test). FOV, field of view. **f**, Relative frequency of CSF-containing channels compared with non-CSF-containing channels ($n=3$). **g**, IVM after indicated intracisternal tracer injection and intravenous dextran ($n=3$–5 per group).

the meninges by quantitative (q)PCR and found them to be 40- to 60-fold higher in mice with meningitis relative to controls injected with aCSF (Extended Data Fig. 3). We next assessed *S. pneumoniae* growth in the blood and CSF using a bacteria colony-forming unit assay 48 h after infection. The blood contained a miniscule amount of *S. pneumoniae*, whereas the CSF contained approximately 10,000-fold more (Fig. 3d), suggesting that, 48 h after infection, bacterial propagation was mostly confined to the meninges. We next sought to visualize *S. pneumoniae* manifestation relative to the skull marrow cavity and skull–dural channel connections. To this end, we injected green fluorescent protein (GFP)-expressing *S. pneumoniae* strain D39V hlpA-GFP into the cisterna magna and adapted an optical clearing protocol[22] to show skull channels, the marrow cavity and adjacent bacterial propagation in the subarachnoidal space. The skull marrow vasculature was stained with intravenously injected fluorescent CD31/Sca1 antibodies and the bone with osteosense, allowing us to identify intact marrow, channels and the CSF space by confocal microscopy (Fig. 3e). To visualize GFP$^+$ *S. pneumoniae*, we employed the timeline established by bioluminescence analysis (Fig. 3a–c). We injected 5×10^3 GFP$^+$ *S. pneumoniae*, or an equal volume of aCSF in controls, and sacrificed mice 48 h later (Fig. 3f). Confocal microscopy of cleared tissue revealed abundant GFP$^+$ bacterial growth in the subarachnoid space of mice with *S. pneumoniae* meningitis, but not controls (Fig. 3e,g and Supplementary Video 3). Three-dimensional (3D) reconstructions document the proximity of GFP$^+$ *S. pneumoniae* to skull channels (Fig. 3h and Supplementary Video 4). In addition to subarachnoidal colonies directly adjacent to dural skull channel openings, bacteria were also present in the skull marrow's extravascular space (Fig. 3h). Taken together, these findings gave rise to the hypothesis that, in meningitis, bacteria may enter the skull bone marrow.

Pneumococcal meningitis propagates to the skull. To test the hypothesis that *S. pneumoniae* entered the skull marrow cavity, we performed in vivo confocal microscopy of the intact skull in mice with meningitis. Mice were imaged 48 h after intracisternal injection with GFP$^+$ *S. pneumoniae* or aCSF in controls. We observed GFP$^+$ bacterial colonies in the skull marrow extravascular spaces of mice with meningitis whereas no such signal was detectable in controls (Fig. 4a and Supplementary Videos 5

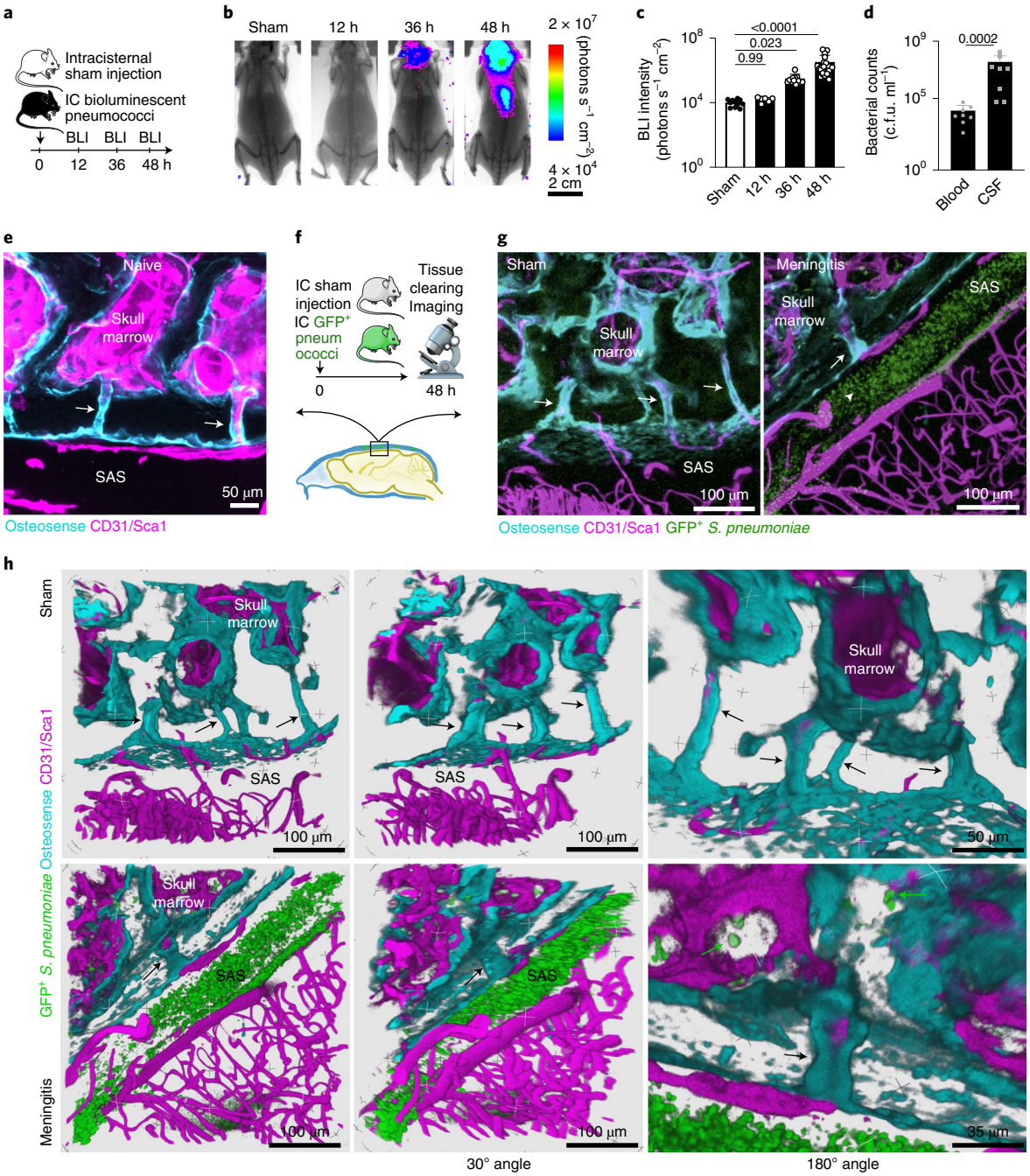

Fig. 3 | Bacterial presence in the meninges and the skull marrow. a, Timeline for bioluminescent *S. pneumoniae* Xen10 meningitis. **b**, BLI of sham controls or mice after intracisternal (IC) injection of *S. pneumoniae* Xen10. **c**, Bacterial load measured by BLI (mean ± s.d.; $n = 11$ sham, 6 at 12 h, 12 at 36 h, 24 at 48 h; *P* values represent a Kruskal–Wallis test with Dunn's multiple comparison test). **d**, Bacterial colony-forming unit assay from blood and CSF at 48 h (mean ± s.d.; $n = 8$; *P* value represents a Mann–Whitney two-sided rank test). **e**, Skull channels after tissue clearing (171 µm, 3 µm per step with 57 steps; $n = 4$ mice from 2 experiments). SAS indicates subarachnoid space. **f**, Tissue-clearing scheme. **g**, Representative *z*-stack images of sham controls (248 µm, 0.75 µm per step with 331 steps) and mice after intracisternal GFP+ *S. pneumoniae* JWV500 (267 µm, 3 µm per step with 89 steps). CD31/Sca1 labels vasculature and osteosense marks bone ($n = 4$ for sham and 6 for meningitis). **h**, Three-dimensional reconstructions highlighting skull channels (arrows) and marrow bacteria (green arrows). The data are pooled from three independent experiments. The upper row indicates control mouse without bacterial injection and the lower row a mouse 48 h after induction of meningitis.

and 6). As this, to our knowledge, could possibly be the first observation of *S. pneumoniae* entering the skull cavity during meningitis, we sought to corroborate these imaging data with orthogonal assays, including bacterial cultures, qPCR for bacterial genes, flow cytometry to detect GFP expressed by bacteria and electron microscopy.

Using an experimental timeline (Fig. 4b) comparable to the imaging experiments described above, we first employed a bacterial colony-forming unit assay to analyze bacterial growth 48 h after intracisternal injection of *S. pneumoniae*. Tibia and skull bone marrow was plated on blood agar plates to accommodate bacterial colony growth, similar to clinical blood cultures. Although bacteria

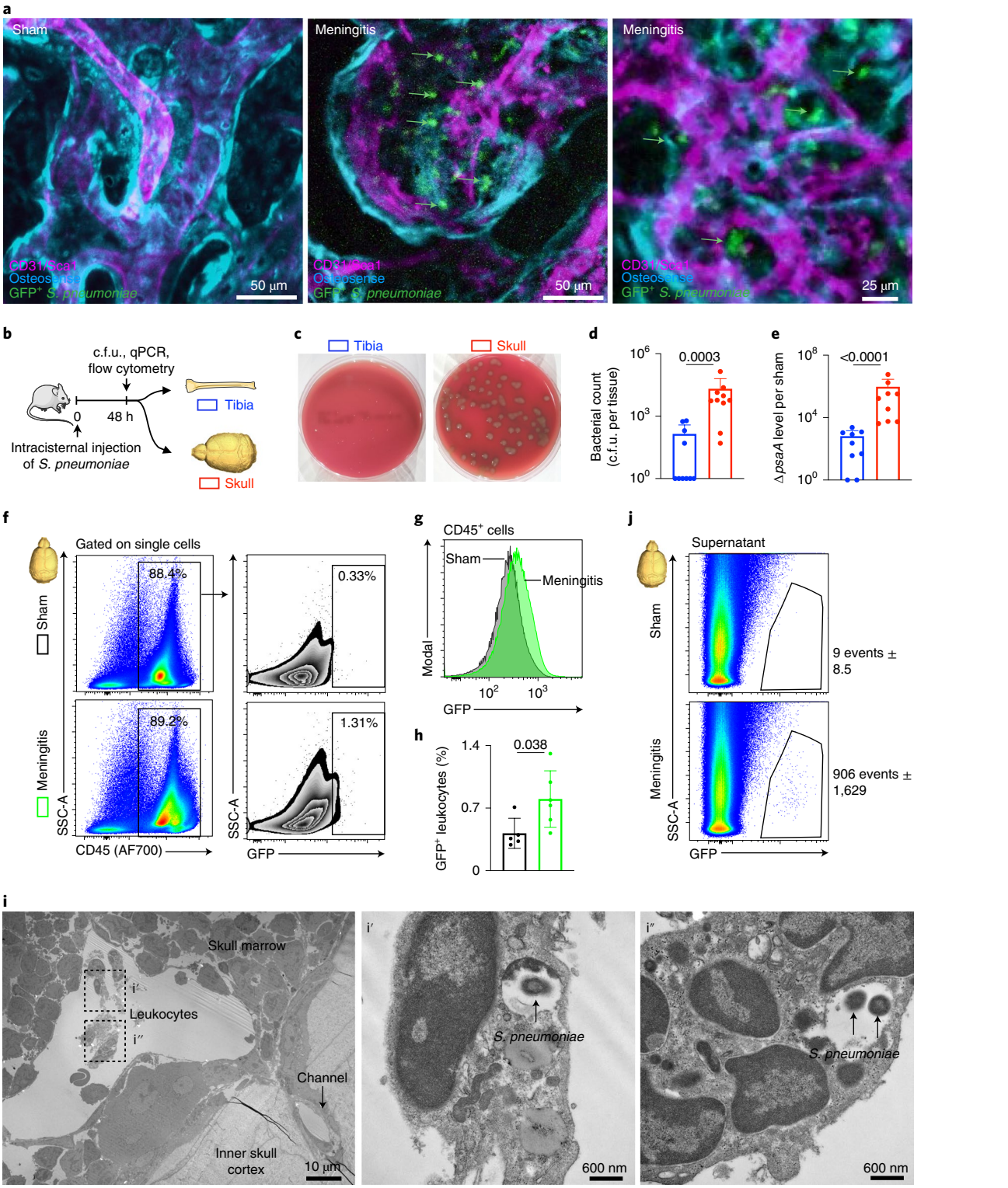

Fig. 4 | Intra- and extracellular bacterial localization in the cranial marrow. a, IVM of skull marrow from sham controls or mice 48 h after intracisternal injection of GFP+ *S. pneumoniae* JWV500 ($n=3$ for sham and 4 for meningitis from 2 independent experiments). **b**, Experimental scheme for **d**–**j**. **c**, Bacterial culture of pneumococcal growth in tibia versus skull. Skull sample contains pooled frontal, parietal and occipital bone. **d**, Quantification of bacterial colony-forming units (mean ± s.d.; $n=10$; *P* value represents a Mann–Whitney two-sided rank test). **e**, *S. pneumoniae* surface adhesion gene (*psaA*) expression in tibia versus skull normalized to sham (mean ± s.d.; $n=9$; *P* value represents a Mann–Whitney two-sided rank test). **f**, Gating strategy for GFP+ CD45+ leukocytes. **g**, Histogram of GFP signal in CD45+ leukocytes obtained from mice with meningitis compared with CD45+ cells from sham controls. **h**, Quantification of GFP+CD45+ cells (mean ± s.d.; $n=5$; *P* value represents an unpaired, two-tailed Student's *t*-test). **i**, TEM of *S. pneumoniae* in the skull marrow. Left: low-magnification view of calvarial marrow depicting a sinusoidal vessel lumen adjacent to a skull channel, the inner skull bone cortex and leukocytes. Right: insets illustrate multiple leukocytes containing *S. pneumoniae* ($n=2$ mice). **j**, Flow cytometric analysis of extracellular GFP+ *S. pneumoniae* in supernatant fraction of tibia and skull ($n=2$ for sham and 4 for meningitis).

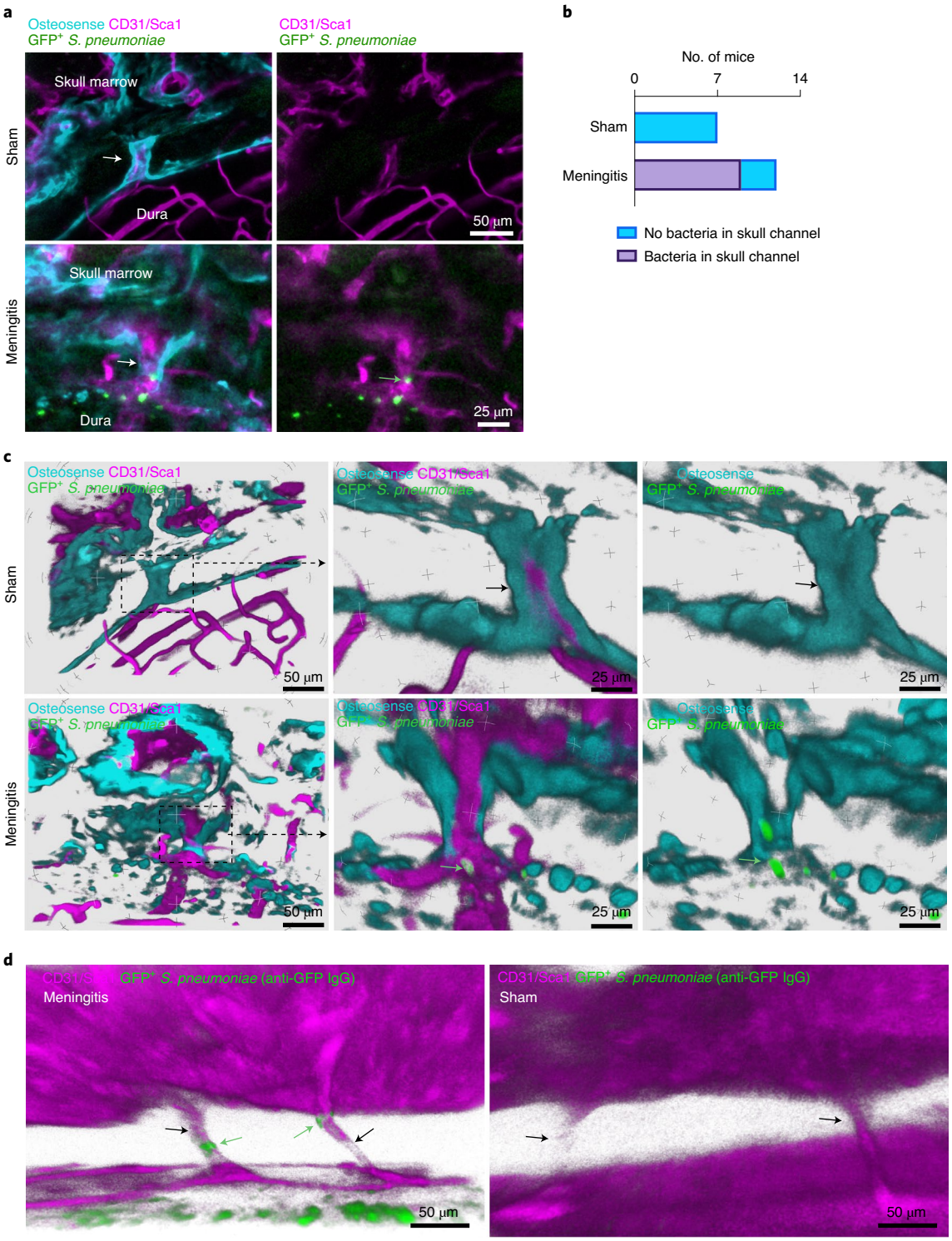

Fig. 5 | Skull channels are conduits for pneumococcal migration into the cranial marrow. a, Whole-mount ex vivo imaging of skull channels in sham controls (132-µm stack, 0.75 µm per step) and mice after intracisternal injection of GFP+ *S. pneumoniae* JWV500 (43-µm stack, 0.75 µm per step; 102-µm stack, 0.75 µm per step). The images depict bacteria (green arrow) in skull channels (white arrow). Osteosense was used to label bone and a CD31/Sca1 cocktail for vasculature ($n = 7$ for sham and 12 for meningitis mice). **b**, Quantification of *S. pneumoniae* GFP signal in skull channels in sham controls and mice with meningitis ($n = 7$ for sham and 12 for mice with meningitis). **c**, Tissue clearing preceded ex vivo imaging of skull channels in sham control or after intracisternal injection of GFP+ *S. pneumoniae* JWV500. Skull channels are visualized using osteosense to label bone and marrow vasculature using a CD31/Sca1 cocktail. The 3D reconstructions show intrachannel *S. pneumoniae* location in meningitis whereas bacteria are absent in sham controls (representative data from three independent experiments). **d**, Whole-mount ex vivo imaging after CUBIC tissue processing for bacterial GFP detection after intracisternal injection of GFP+ *S. pneumoniae* JWV500. CUBIC protocol (described in Methods) was followed by immunostaining for bacterial GFP. Bone marrow vasculature was labeled in vivo with CD31/Sca1 ($n = 2$ mice). The green arrows indicate bacteria and the black skull channels. EM, Electron microscopy; IgG, immunoglobulin G; PV, perivascular.

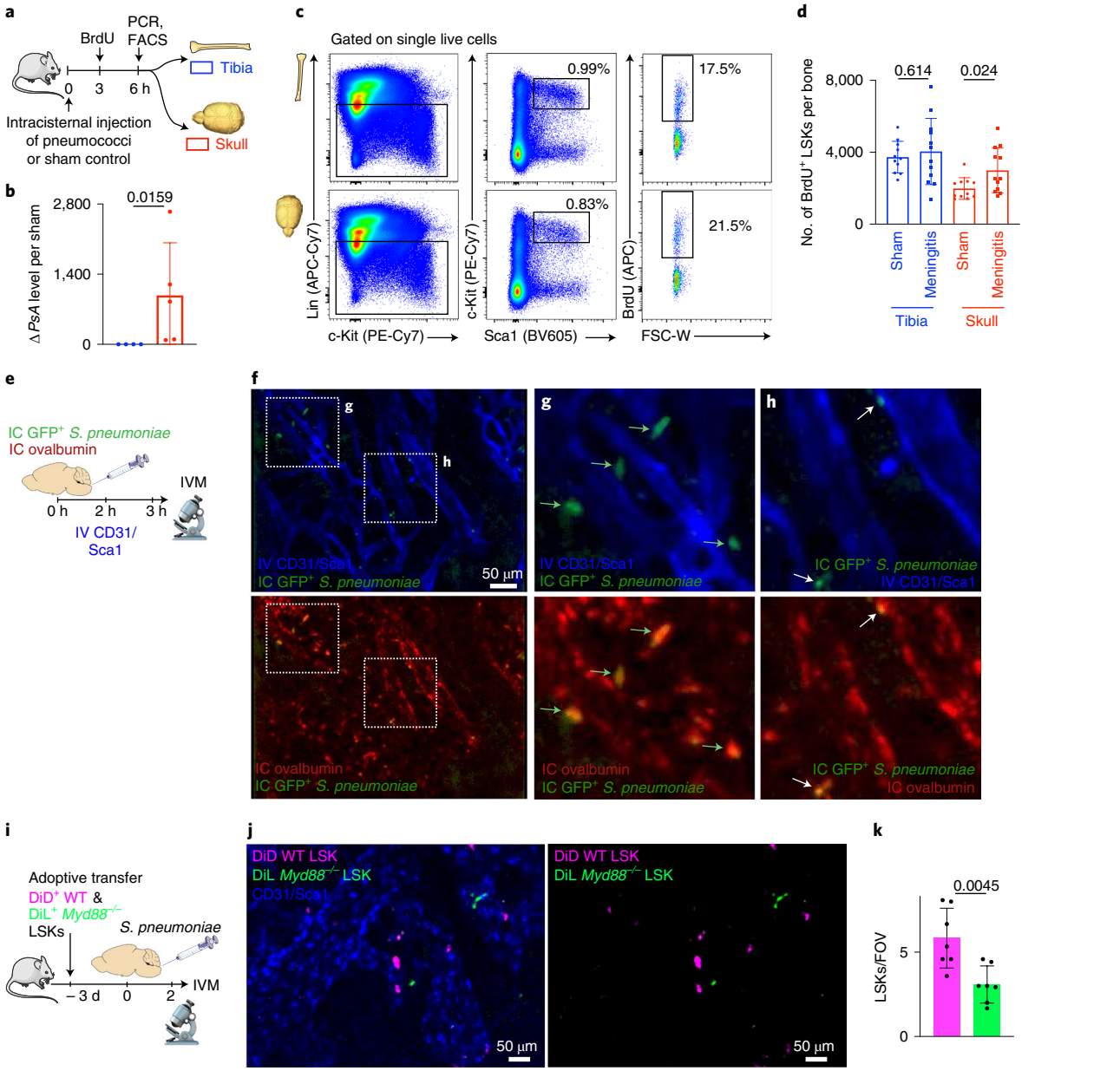

Fig. 6 | Bacterial meningitis induces LSK proliferation in the skull. a, Outline for experiments **b**–**d**. **b**, The qPCR detection of *S. pneumoniae psaA* gene expression in tibia versus skull normalized to sham controls (mean ± s.d.; $n = 4$; *P* value represents a Mann–Whitney two-tailed rank test). **c**, Flow cytometry gating. **d**, Quantification of BrdU+ LSK hematopoietic progenitors (mean ± s.d.; $n = 11$ for sham and 12 for meningitis; *P* values represent unpaired, two-tailed Student's *t*-tests). **e**, Experimental outline. **f**, IVM of skull marrow at 4–6 h after intracisternal injection of GFP+ *S. pneumoniae* JWV500. Vasculature was labeled with CD31/Sca1 and CSF with intracisternal ovalbumin. **g**, Inset depicting large GFP+ bacterial areas (arrows) (**f** and **g** are representative data from two independent experiments). **h**, Inset showing smaller GFP+ areas, presumably bacterial colonies ($n = 2$). **i**, Experimental outline. Flow-sorted LSKs underwent membrane staining encoding their genotype; *Myd88*$^{-/-}$ (green) and wild-type LSKs (magenta) were transferred to a recipient mouse in which meningitis was induced. IVM was done 48 h after infection. **j**, IVM images showing fewer *Myd88*$^{-/-}$ LSK compared with wild-type control LSKs. **k**, Quantification of LSKs (mean ± s.d.; $n = 7$ recipient mice; *P* value represents an unpaired, two-tailed Student's *t*-test).

were almost undetectable in tibial marrow, bacterial colonies grew from the skull marrow preparations (Fig. 4c,d). As only viable bacteria can divide, this finding documents live bacteria being present in the skulls of mice with meningitis. We next compared skull and tibial marrow using qPCR analysis for the bacterial gene *psaA*, which is not expressed in mice. Skull samples from mice with meningitis contained markedly higher levels of *psaA* transcript compared with the tibia (Fig. 4e), confirming the presence of *S. pneumoniae* within the skull marrow. Furthermore, we performed flow cytometric analysis on skull marrow isolated from mice after intracisternal injection of GFP+ *S. pneumoniae*. In addition to detecting bacterial presence, flow cytometry also determined whether bacteria are located inside cells. The skulls of mice with meningitis showed substantial numbers of CD45+GFP+ leukocytes, which were largely absent in the skulls of control mice (Fig. 4f). We document the observed fraction of bacteria-containing leukocytes in a right-shifted GFP histogram in CD45+ leukocytes obtained from the skull marrow of mice with meningitis, compared with controls injected with aCSF (Fig. 4g,h). The presence of intracellular bacteria in the skull bone marrow was confirmed by electron microscopy (Fig. 4i). We also analyzed the

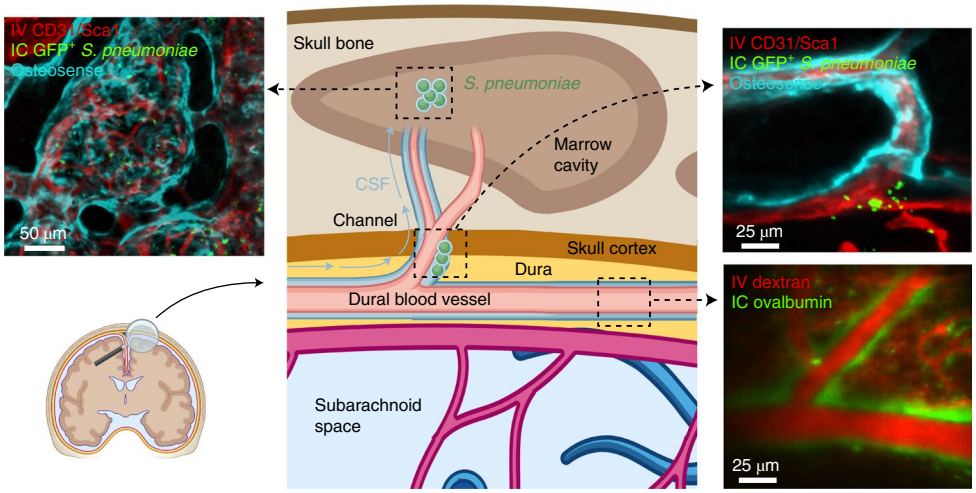

Fig. 7 | Summary cartoon. CSF outflow occurs via dural perivascular spaces through skull channels into the cranial marrow. This route is usurped by bacteria during meningitis.

cell-free supernatant of bone marrow suspensions after high-speed centrifugation by flow cytometry. In the skull marrow supernatant obtained from mice that received an intracisternal GFP$^+$ *S. pneumoniae* injection, we noted abundant bacteria that were absent in controls (Fig. 4j). Taken together, the intravital imaging observation of bacteria in the skull marrow of mice with meningitis was confirmed by four independent assays, all supporting the notion that bacteria can propagate from the meninges to the skull marrow.

Skull channels are conduits for *S. pneumoniae* into the marrow. To directly evaluate whether *S. pneumoniae* reaches the skull marrow by transiting skull channels from the dura, we performed ex vivo confocal microscopy of tissue-cleared skull preparations containing intact brain tissue 48 h after intracisternal injection of either GFP$^+$ *S. pneumoniae* or aCSF in controls. The *z*-stack projections of skull channels revealed the presence of GFP$^+$ *S. pneumoniae* inside skull channels (Fig. 5a). We found that 75% of mice with meningitis showed bacterial GFP signal in their skull channels, whereas control animals without meningitis lacked any sign of *S. pneumoniae* (Fig. 5b). The 3D reconstructions of skull channels revealed extravascular GFP localization within the channels of mice with meningitis, but not in controls (Fig. 5c and Supplementary Videos 7 and 8). As a complementary approach to imaging bacterial GFP directly, we adapted optical clearing methods to search for GFP$^+$ *S. pneumoniae* in deeper tissue areas[22]. Whole-mount confocal microscopy of CUBIC-processed meningitis specimens revealed a striking pattern of anti-GFP staining within skull channels (Fig. 5d). Skulls from control mice showed no GFP signal in the dura, channels or marrow (Fig. 5d and Extended Data Fig. 3d). Collectively, these data demonstrate two previously unknown phenomena: (1) during meningitis, bacteria enter the skull marrow through skull channels from the dura, and (2) bacterial influx through channels into the marrow occurs via a perivascular route, similar to CSF outflow into the marrow described in Fig. 2. However, our data do not exclude that bacteria may also invade the vasculature and migrate through channels intravascularly. Furthermore, it remains to be experimentally determined whether different infection routes influence bacterial emigration through skull channels.

***S. pneumoniae* propagation in the CSF induces skull hematopoiesis.** Having defined the route by which CSF and *S. pneumoniae* transit skull channels via perivascular passage and arrive within the skull marrow, we next tested how this signaling affects hematopoiesis. Specifically, we devised an experimental timeline to test whether intracisternal injection of *S. pneumoniae* elicits a hematopoietic response in skull marrow before distal tibial bone marrow (Fig. 6a). We hypothesized that skull marrow changes may be observable as early as 6 h after intracisternal injection of *S. pneumoniae*. Our previous work, which supports this timeline, had identified a rapid skull marrow response in an ischemic stroke model[8]. We first performed qPCR to clarify whether bacteria enter the skull at this early timepoint and found that the bacterial gene *psaA* was indeed expressed in the skull but not the tibia 6 h after intracisternal infection (Fig. 6b). We then analyzed bromodeoxyuridine (BrdU) incorporation into Lin$^-$Sca1$^+$c-kit$^+$ (LSK) hematopoietic progenitors in the skull and the remote tibia by flow cytometry to determine whether *S. pneumoniae* had altered LSK proliferation. Mice with meningitis had significantly increased BrdU$^+$ LSKs in the adjacent skull but not in the remote tibial marrow (Fig. 6c,d). The number of BrdU$^+$ LSKs and BrdU$^+$ common myeloid progenitors (CMPs) increased in the skull 24 h after bacterial infection (Extended Data Fig. 4). To confirm our observation that elevated LSK proliferation associates with direct local *S. pneumoniae* skull infiltration, we used confocal IVM to image GFP$^+$ *S. pneumoniae* progression into the skull marrow 3 h after infection. Exploring whether bacteria were located in the skull marrow's CSF-containing compartment, we co-injected fluorescently labeled ovalbumin at the time of bacterial infection (Fig. 6e). We noted large extravascular GFP$^+$ signal clusters within the marrow that were co-labeled with IC injected ovalbumin (Fig. 6f,g), a result suggesting that cells contained bacteria. In addition, we observed smaller extravascular GFP$^+$ areas that also colocalized with the CSF tracer ovalbumin and we interpreted these as extracellular bacteria (Fig. 6h).

It is interesting that we detected that skull myeloid cell numbers declined 24 h after induction of meningitis (Extended Data Fig. 5). When viewed together with increased skull hematopoietic stem and progenitor cell (HSPC) proliferation, that is, higher leukocyte production, and previous data[23–28] indicating neutrophil and monocyte infiltration of infected meninges and the CSF, the concomitant decrease of skull and increase of meningeal leukocytes (Extended Data Fig. 6) indicated that skull-derived leukocytes may migrate to the infected meninges. To test this experimentally, we tracked skull leukocytes in mice using skull-specific bone marrow transplantation[11]. To this end, the heads of CD45.2 mice were irradiated whereas their bodies were shielded, which was followed by transplantation of CD45.1 bone marrow (Extended Data Fig. 7a).

As previously reported[11], this procedure led to preferential seeding of transplanted CD45.1 marrow in the skull whereas the nonirradiated marrow remained CD45.2$^+$ (Extended Data Fig. 7b,c). Two days after induction of meningitis, we detected CD45.1$^+$ leukocytes in infected meninges at a chimerism that exceeded the chimerism in blood (Extended Data Fig. 7d,e), supporting that skull-derived leukocytes migrate to the meninges.

Finally, as bacterial sensing occurs via toll-like receptors and the adaptor molecule Myd88 (ref. [29]), we sought to test whether such sensing is involved in skull LSK expansion observed in mice with meningitis. Thus, we isolated 40,000 LSKs from wild-type and *Myd88*$^{-/-}$ donor mice, labeled them with spectrally resolved membrane dyes and co-transferred this dual color mix into wild-type recipients, which were then infected with an intracisternal injection of bacteria (Fig. 6i). *Myd88*$^{-/-}$ hematopoietic progenitors exhibit normal frequencies and bone marrow homing if transferred into nonirradiated recipients[30], which we confirmed by flow cytometry (Extended Data Fig. 8a–f). Two days after infection, using IVM enumeration of wild-type and knockout progenitors in the skull, we detected approximately twofold fewer *Myd88*$^{-/-}$ LSKs than wild-type LSKs (Fig. 6j,k). Corroborating these data with flow cytometry as an alternative method, we did not detect increased HSPC proliferation in the skull of *Myd88*$^{-/-}$ mice with meningitis (Extended Data Fig. 8g–j). We analyzed progenitor proliferation in *Myd88*$^{-/-}$ mice at 12 h, an intermediate timepoint between the observed increased LSK proliferation in wild-type mice at 6 and 24 h. These data suggest that toll-like receptor signaling in skull HSPCs is required for their expansion during meningitis, and we speculate that hematopoietic progenitor cells directly sense bacteria that have migrated to the skull marrow. However, other mechanisms, perhaps including cytokine signaling of meningeal leukocytes, may also alert hematopoietic cells in the skull. In sum, our data point to a process by which IC injected bacteria co-opt a perivascular CSF passage into the skull marrow, inciting a skull-specific increase in LSK proliferation that precedes changes in distal tibial bone marrow (Fig. 7).

Discussion

Every day, the human ventricular choroid plexus produces most of the 500 ml of CSF that provides a protective environment for the brain and receives waste from brain interstitial fluid through exchange with the glymphatic system. CSF outflow occurs via several routes[6]: (1) through arachnoidal villi described >100 years ago[31], (2) along spinal and cranial nerves and (3) through dural lymphatics to cervical lymph nodes[32,33]. Our work establishes an additional outward signaling pathway facilitated by CSF outflow along dural vessels that transit skull channels into the marrow. However, we did not determine the ultimate fate of CSF after it enters the bone via the skull channels. Other open questions include whether perivascular bacterial migration faces size constraints and whether bacteria traverse skull channels predominantly by themselves or inside leukocytes.

Given that skull channel CSF outflow—similar to dural lymphatic vessels—connects to a site of leukocyte abundance, it probably also serves immune surveillance. We speculate that while dural lymphatics alert adaptive immune cells residing in lymph nodes, skull channel signaling may primarily involve innate immune cells produced locally in the calvarial marrow. This reasoning is supported by immune cell migration through skull channels in steady-state, nerve crush injury, experimental autoimmune encephalomyelitis[11] (a mouse model of multiple sclerosis) and chemically induced meningitis[8]. When considered together, CSF outflow to skull marrow and leukocyte migration toward the meninges embody components of a local immune cell supply chain that bypasses systemic circulation.

Our work introduces CSF sampling via the skull marrow, in which immune sentinels are highly abundant. Perhaps related to this discovery, recent human imaging studies showed a robust inflammatory signal in skull bone marrow overlying repeatedly abnormal brain cortex in patients with migraine[34] and in other pathologies[35]. Although we demonstrate the relevance of CSF outflow to the skull in the setting of bacterial meningitis in mice, such surveillance may also shape the immune response in chronic inflammatory CNS disorders such as Alzheimer's disease and multiple sclerosis. In addition, as previous work described the contributions of marrow-derived myeloid cells to recovery from spinal cord injury[4,36] and stroke[37], skull marrow may also participate in those settings. As dura–marrow connections similar to skull channels exist in vertebrae[38], the question arises if vertebral marrow reacts in synchrony with the skull or more like the remote tibial marrow. Generally, the skull marrow warrants closer scrutiny due to its proximity to and crosstalk with the meninges and the CNS. Constant sampling of CSF outflow suggests that the skull marrow state may reflect brain health and that the skull marrow has a prominent role in regulating CNS inflammation.

Online content

Any methods, additional references, Nature Research reporting summaries, extended data, supplementary information, acknowledgements, peer review information; details of author contributions and competing interests; and statements of data and code availability are available at https://doi.org/10.1038/s41593-022-01060-2.

Received: 19 October 2021; Accepted: 23 March 2022;
Published online: 02 May 2022

References

1. Ransohoff, R. M., Kivisakk, P. & Kidd, G. Three or more routes for leukocyte migration into the central nervous system. *Nat. Rev. Immunol.* **3**, 569–581 (2003).
2. Engelhardt, B., Vajkoczy, P. & Weller, R. O. The movers and shapers in immune privilege of the CNS. *Nat. Immunol.* **18**, 123–131 (2017).
3. Gres, V., Kolter, J., Erny, D. & Henneke, P. The role of CNS macrophages in streptococcal meningoencephalitis. *J. Leukoc. Biol.* **106**, 209–218 (2019).
4. Greenhalgh, A. D. et al. Peripherally derived macrophages modulate microglial function to reduce inflammation after CNS injury. *PLoS Biol.* **16**, e2005264 (2018).
5. Wilson, E. H., Weninger, W. & Hunter, C. A. Trafficking of immune cells in the central nervous system. *J. Clin. Invest.* **120**, 1368–1379 (2010).
6. Proulx, S. T. Cerebrospinal fluid outflow: a review of the historical and contemporary evidence for arachnoid villi, perineural routes, and dural lymphatics. *Cell. Mol. Life Sci.* **78**, 2429–2457 (2021).
7. Plog, B. A. & Nedergaard, M. The glymphatic system in central nervous system health and disease: past, present, and future. *Annu. Rev. Pathol.* **13**, 379–394 (2018).
8. Herisson, F. et al. Direct vascular channels connect skull bone marrow and the brain surface enabling myeloid cell migration. *Nat. Neurosci.* **21**, 1209–1217 (2018).
9. Cai, R. et al. Panoptic imaging of transparent mice reveals whole-body neuronal projections and skull-meninges connections. *Nat. Neurosci.* **22**, 317–327 (2019).
10. Brioschi, S. et al. Heterogeneity of meningeal B cells reveals a lymphopoietic niche at the CNS borders. *Science* **373**, eabf9277 (2021).
11. Cugurra, A. et al. Skull and vertebral bone marrow are myeloid cell reservoirs for the meninges and CNS parenchyma. *Science* **373**, eabf7844 (2021).
12. Lovato, L. et al. Related B cell clones populate the meninges and parenchyma of patients with multiple sclerosis. *Brain* **134**, 534–541 (2011).
13. Iliff, J. J. et al. A paravascular pathway facilitates CSF flow through the brain parenchyma and the clearance of interstitial solutes, including amyloid beta. *Sci. Transl. Med.* **4**, 147ra111 (2012).
14. Harling-Berg, C., Knopf, P. M., Merriam, J. & Cserr, H. F. Role of cervical lymph nodes in the systemic humoral immune response to human serum albumin microinfused into rat cerebrospinal fluid. *J. Neuroimmunol.* **25**, 185–193 (1989).
15. Harris, M. G. et al. Immune privilege of the CNS is not the consequence of limited antigen sampling. *Sci. Rep.* **4**, 4422 (2014).
16. Stanton, E. H. et al. Mapping of CSF transport using high spatiotemporal resolution dynamic contrast-enhanced MRI in mice: effect of anesthesia. *Magn. Reson. Med.* **85**, 3326–3342 (2021).
17. Xavier, A. L. R. et al. Cannula Implantation into the cisterna magna of rodents. *J. Vis. Exp.* **135**, 57378 (2018).

18. Courties, G. et al. Ischemic stroke activates hematopoietic bone marrow stem cells. *Circ. Res.* **116**, 407–417 (2015).
19. Vandoorne, K. et al. Imaging the vascular bone marrow niche during inflammatory stress. *Circ. Res.* **123**, 415–427 (2018).
20. Mook-Kanamori, B., Geldhoff, M., Troost, D., van der Poll, T. & van de Beek, D. Characterization of a pneumococcal meningitis mouse model. *BMC Infect. Dis.* **12**, 71 (2012).
21. van de Beek, D., de Gans, J., Tunkel, A. R. & Wijdicks, E. F. Community-acquired bacterial meningitis in adults. *N. Engl. J. Med.* **354**, 44–53 (2006).
22. Tainaka, K. et al. Chemical landscape for tissue clearing based on hydrophilic reagents. *Cell Rep.* **24**, 2196–2210.e9 (2018).
23. Guarner, J. et al. Neutrophilic bacterial meningitis: pathology and etiologic diagnosis of fatal cases. *Mod. Pathol.* **26**, 1076–1085 (2013).
24. Engelen-Lee, J. Y., Koopmans, M. M., Brouwer, M. C., Aronica, E. & van de Beek, D. Histopathology of listeria meningitis. *J. Neuropathol. Exp. Neurol.* **77**, 950–957 (2018).
25. Rua, R. et al. Infection drives meningeal engraftment by inflammatory monocytes that impairs CNS immunity. *Nat. Immunol.* **20**, 407–419 (2019).
26. Nau, R. et al. Granulocytes in the subarachnoid space of humans and rabbits with bacterial meningitis undergo apoptosis and are eliminated by macrophages. *Acta Neuropathol.* **96**, 472–480 (1998).
27. Mildner, A. et al. $Ly^{-}6G^{+}CCR2^{-}$ myeloid cells rather than $Ly^{-}6ChighCCR2^{+}$ monocytes are required for the control of bacterial infection in the central nervous system. *J. Immunol.* **181**, 2713–2722 (2008).
28. Djukic, M. et al. Circulating monocytes engraft in the brain, differentiate into microglia and contribute to the pathology following meningitis in mice. *Brain* **129**, 2394–2403 (2006).
29. Lind, N. A., Rael, V. E., Pestal, K., Liu, B. & Barton, G. M. Regulation of the nucleic acid-sensing Toll-like receptors. *Nat. Rev. Immunol.* **22**, 224–235 (2022).
30. Rahman, A. H. & Turka, L. A. MyD88 expression in stem cells regulates hematopoietic reconstitution following bone marrow transplantation. *J. Immunol.* **182**, 138.16 (2009).
31. Weed, L. H. Studies on cerebro-spinal fluid. No. III: the pathways of escape from the subarachnoid spaces with particular reference to the arachnoid villi. *J. Med Res* **31**, 51–91 (1914).
32. Louveau, A. et al. Structural and functional features of central nervous system lymphatic vessels. *Nature* **523**, 337–341 (2015).
33. Aspelund, A. et al. A dural lymphatic vascular system that drains brain interstitial fluid and macromolecules. *J. Exp. Med.* **212**, 991–999 (2015).
34. Hadjikhani, N. et al. Extra-axial inflammatory signal in parameninges in migraine with visual aura. *Ann. Neurol.* **87**, 939–949 (2020).
35. Ringstad, G. & Eide, P. K. Molecular trans-dural efflux to skull bone marrow in humans with cerebrospinal fluid disorders. *Brain* https://doi.org/10.1093/brain/awab388 (2021).
36. Shechter, R. et al. Infiltrating blood-derived macrophages are vital cells playing an anti-inflammatory role in recovery from spinal cord injury in mice. *PLoS Med.* **6**, e1000113 (2009).
37. Gliem, M., Schwaninger, M. & Jander, S. Protective features of peripheral monocytes/macrophages in stroke. *Biochim. Biophys. Acta* **1862**, 329–338 (2016).
38. Yao, H. et al. Leukaemia hijacks a neural mechanism to invade the central nervous system. *Nature* **560**, 55–60 (2018).

Publisher's note Springer Nature remains neutral with regard to jurisdictional claims in published maps and institutional affiliations.

© The Author(s), under exclusive licence to Springer Nature America, Inc. 2022

Methods

Mice. Mice were housed under certified pathogen-free conditions at Massachusetts General Hospital's Center for Comparative Medicine. All experiments were conducted in accordance with the Institutional Animal Care and Use Committee's approval (protocol nos. 2005N000306, 2019N000203, 2009N000085 and 2007N000148). Male and female C57BL/6 (all wild-type animals are derived from a CD45.2 background; Jackson Lab, catalog no. JAX 000664) aged 10–16 weeks were used for all experiments. Male *Myd88*$^{-/-}$ (Jackson Lab, catalog no. 009088) and CD45.1 (Jackson Lab, catalog no. 002014) ordered at age 8 weeks were also used for transplantation experiments. Mice were provided rodent chow and water and allowed to acclimate for 1 week before experimentation. All mice were group housed on a 12 h:12 h light:dark cycle at 22 °C with unlimited access to food and water Animals were assigned to experimental groups randomly and experiments were performed in a blinded fashion.

S. pneumoniae. *S. pneumoniae* strain JWV500 (D39V hlpA-gfp_Cam^r; serotype 2) was generously provided by J.-W. Veening and prepared as previously described[39]. *S. pneumoniae* Xen10 (serotype 3) was purchased from Caliper LifeSciences. GFP$^+$ *S. pneumoniae* and *S. pneumoniae* Xen10 were cultured in brain–heart infusion broth (BHI) containing 4.5 μg ml^{-1} of chloramphenicol or 200 μg ml^{-1} of kanamycin, respectively. *S. pneumoniae* strains were cryopreserved in BHI with 30% glycerol, thawed the day before the experiment in a 37 °C water bath and diluted in fresh BHI with the antibiotic. Bacterial doses between 1:10^3 and 1:10^6 colony-forming units (c.f.u.) were used, depending on experimental design. Optical densities (at 600 nm) were used for all bacterial experiments to approximate colony-forming units, but serial plating dilutions confirmed actual colony-forming units on BHI agar.

Micro-CT protocol and channel analysis. Samples were imaged using a high-resolution CT scanner (μCT40, Scanco Medical AG). Data were acquired using a 6-μm^3 isotropic voxel size, 70-kVp peak X-ray tube intensity, 114-μA X-ray tube current and 200-ms integration time, and were subjected to Gaussian filtration. Image renderings were done in Amira (FEI). Three regions of interest in the midline from the right frontal, parietal and occipital bones were identified and analyzed for each individual mouse. Similar sized volumes with dimensions of 1.25 mm to 4 mm depending on bone anatomy were analyzed for channel length, width and density. These areas were then viewed in an oblique coronal orientation to visually identify channels at an identical brightness setting for the fields of view selected. The magnifying tool was used to select channels that were identified based on their appearance. Identified channels were first counted and then given unique identifiers. Next, a line was drawn, starting in the first coronal section at the interior skull channel opening into the final plane where the channel reached the marrow cavity. A line perpendicular to this channel axis was drawn to determine the width of each channel.

Cisterna magna injections. Mice were anesthetized by isoflurane inhalation (3–4% induction, 1–2% maintenance), injected with buprenorphine (0.1 mg kg^{-1} before surgery and every 12 h until sacrifice), followed by hair removal from the back of the neck (Nair). We used a thermometer and feedback-controlled heating blanket (Harvard Apparatus) to maintain body temperature at 37 °C. Mice were fixed on a stereotaxic frame (Harvard Apparatus) with the neck angled downward for optimal cisterna magna exposure, and eye ointment (Dechra) was applied to prevent indirect damage during surgery. An approximately 4-mm vertical skin incision was made at the back of the neck, and the junction between the skull and the first vertebra was exposed by bluntly separating the overlaying muscles[17]. A 30-μm inner diameter glass micropipette (Fivephoton Biochemicals, catalog no. MGM-1C-30-30) attached to a ultra-precise micro-manipulator (Stoelting) loaded with 5 μl of aCSF (119 mM NaCl, 26.2 mM $NaHCO_3$, 2.5 mM KCl, 1 mM NaH_2PO_4, 1.3 mM $MgCl_2$ and 2.5 mM $CaCl_2$) containing 5×10^3 or 1×10^5 *S. pneumoniae* was injected through the dura toward the cerebellopontine angle. For sham controls, 5 μl of sterile aCSF was injected. These injections were administered at a speed of 1 μl min^{-1} with a micro-syringe pump (Harvard Apparatus) and a customized Hamilton Company syringe (10-μl volume; 3-point style; 20 gauge; 10-mm needle length). To prevent backflow-induced variability among individual injections, the needle was retracted incrementally over the course of 10–30 min. After the injection, the incision and surrounding area were treated with Terramycin (oxytetracycline) ointment (Zoetis, Inc.). The incision was sutured with a 5/0 silk suture (Ethilon).

Surgical preparation for two-photon IVM (described below) was similarly performed with slight modifications to minimize pain and distress over longer imaging periods. Mice were anesthetized with 3% isoflurane, placed on a stereotactic surgery frame (Harvard Apparatus) and then maintained on 1.5% isoflurane in 100% oxygen. Mice were also treated with 0.05 mg per 100-g body weight of glycopyrrolate (Baxter, Inc.), 0.025 mg per 100-g body weight of dexamethasone (Phoenix Pharm, Inc., catalog no. 07-808-8194) and 0.5 mg per 100-g body weight of ketoprofen (Zoetis, Inc.). Glycopyrrolate and ketoprofen were injected intramuscularly, whereas dexamethasone was injected subcutaneously. Bupivacaine (0.1 ml, 0.125%; Hospira, Inc.) was subcutaneously administered at the incision site to provide a local nerve block. Animals were provided with 1 ml per 100-g 5% (w:v) glucose in physiological saline subcutaneously every hour during the procedure. We used a thermometer and feedback-controlled heating blanket (FHC, catalog no. 40-90-8D DC) to maintain body temperature at 37 °C. The head and neck were shaved and washed with 70% (v:v) ethanol and iodine solution (AgriLabs). An intracisternal injection was performed as described above. After the injections, the exposed tissue was sealed with cyanoacrylate adhesive (Loctite) and dental cement (Co-Oral-Ite Dental).

Skull marrow preparation and confocal microscopy. For in vivo imaging, the mouse head was shaved and held in a stereotactic skull holder (Harvard Apparatus). Calvarial bone marrow was exposed, as previously described[18], by incising a skin flap and then applying glycerol (Sigma-Aldrich) to prevent tissue drying. Skull marrow microscopy was performed with a single-photon confocal microscope (IV 100, Olympus) equipped with IV10-ASW 01.01.00.05 software (Olympus). A field of view at ×4 magnification covers a 2,290 × 2,290 μm^2 area whereas ×20 magnification covers a 458 × 458 μm^2 area consisting of 512 × 512 pixels. For ex vivo skull preparation and imaging after tissue clearing, mice were humanely sacrificed. Then, the head with brain intact was split longitudinally along the sagittal sinus and fixed for 1 h in 4% paraformaldehyde (PFA), after which tissue was washed and subjected to clearing in RapiClear 1.49 (SunJinLab) for 1–2 h, depending on sample size. Specimens were then mounted on a customized tissue holder with a hanging, mounted coverslip (Harvard Apparatus). As indicated in specific figure panels with regard to the intravenous injection timing (retro-orbital intravenous injection, 100-μl total volume in phosphate-buffered saline (PBS)), mice received the following reagents for IVM and ex vivo imaging: 30 μl of CD31-AF647 (BioLegend, MEC13.3), 30 μl of CD31-PE (BioLegend, clone MEC13.3), 30 μl of Sca1-AF647 (BioLegend, clone D7), 30 μl of Sca1-PE (BioLegend, clone D7) and 100 μl of Osteosense 750EX (Perkin Elmer, catalog no. NEV10053EX), as previously described[19,40].

Two-photon IVM and ex vivo imaging. Mice were anesthetized and placed on a customized stereotactic frame. During imaging, anesthesia was maintained with ~1.5% isoflurane in 100% oxygen, with small adjustments to maintain the respiratory rate at ~1 Hz. To fluorescently label the microvasculature, Texas Red Dextran (40 μl, 2.5%, molecular mass (M_r) = 70,000 kDa, Thermo Fisher Scientific) in saline was injected retro-orbitally immediately before imaging. The 3D datasets of the calvarial bone marrow, meninges, meningeal vasculature and CSF transport were obtained using a customized two-photon excitation microscope. Imaging was done using 830-nm, 120-fs pulses from a Ti:Sapphire laser oscillator (Spectra-Physics InSight X3). The laser beam was scanned by polygon scanners (30 frames s^{-1}) and focused into the sample using a ×60 water-immersion objective lens for high-resolution imaging (numerical aperture of 1.1, Olympus). The emitted fluorescence was detected on photomultiplier tubes through the following emission filters: 400/60 nm for second harmonic generation, 525/50 nm for Alexa-488/FITC and 605/50 nm for Texas Red. Laser scanning and data acquisition were controlled by customized software. Stacks of images were spaced at 1 μm axially.

CSF tracing. Mice were injected with fluorescent CSF tracers, which were reconstituted in aCSF at a concentration of 0.5%. For two-photon IVM and two-photon ex vivo experiments, mice were IC injected with 2,000-kDa FITC–Dextran (Thermo Fisher Scientific, catalog no. D7137), 70-kDa Texas Red Dextran (Thermo Fisher Scientific, catalog no. D1830) and AF647-Ovalbumin (Invitrogen, catalog no. O34784). For confocal microscopy, mice were injected with AF488-Ovalbumin (Sigma-Aldrich, catalog no. O34781) and AF647-Ovalbumin (Sigma-Aldrich, catalog no. O34784) reconstituted in a 5-μl volume of aCSF at an injection speed of 1 μl min^{-1}, which changes intracranial pressure only very mildly and for a brief period of time[41]. We examined CSF trafficking in the marrow by ex vivo imaging as described[8]. The *z*-stacks of marrow–channel–dural spaces were acquired in vivo, after which mice were euthanized at the indicated timepoints following intracisternal injection of tracer. A piece of frontal bone containing marrow was then excised, preserving the integrity of the dura and the bone marrow cavities. The excised specimen was inverted and rapidly transferred into an aCSF bath or stage mounted for whole-mount imaging. Tibia bone was embedded in OCT medium (TissueTek) and snap-frozen. Cortical bone was shaved on a crystotat until the marrow was visible.

TEM. Skull samples were collected for TEM as described above with the following modifications. Cardiac perfusion with PBS was followed by 20 ml of Karnovsky's fixative (0.1 M sodium cacodylate, 2.5% glutaraldehyde and 2% PFA). The skull was excised and trimmed to contain the frontal, parietal and occipital bones, and fixed for 3 h in Karnovsky's fixative followed by 48-h fixation at 4 °C. Marrow-containing 2× 4-mm pieces were decalcified over 2 weeks in 140 mM EDTA, pH 7.4 (Boston BioProducts). Specimens were fixed in 1% glutaraldehyde in cacodylate buffer overnight at 4 °C. Specimens were infiltrated in 1% osmium tetroxide, rinsed in cacodylate buffer and then dehydrated. Samples were then incubated in a 1:1 mix of propylene oxide and Eponate resin (Ted Pella). The following day, specimens were incubated for at least 3 h in 100% Eponate resin, then placed into molds with 100% Eponate resin and allowed to polymerize in a 60 °C oven. Semi-thin sections (1 μm) were collected on to slides and stained with 0.1% Toluidine Blue to preview channels. Then, 70-nm sections were cut using a Leica EM UC7 ultramicrotome,

collected on to formvar-coated grids, stained with 2% uranyl acetate and Reynold's lead citrate, and examined in a JEOL JEM 1011 transmission electron microscope at 80 kV. Images were collected using an AMT digital imaging system with proprietary image capture software (Advanced Microscopy Techniques).

Tissue clearing. This protocol was adapted from Tainaka and colleagues[22] to detect GFP expressed by *S. pneumoniae*. Mice were first IC injected with GFP$^+$ *S. pneumoniae* as described above for analysis 48 h after infection. Then 1 h before sacrifice, mice were retro-orbitally injected with a CD31/Sca1-AF647 cocktail to label the vasculature. Skull bones were fixed overnight in 4% PFA with shaking at 4 °C and subsequently washed 5× for 10 min per wash in PBS on a bench-top shaker (400 r.p.m.). Skull samples were delipidized/decolored in CUBIC-L solution (10 wt% of *N*-butyldiethanolamine (Tokyo Chemical Industry, catalog no. 0414), 10 wt% Triton X-100 (Sigma-Aldrich)) for 4 d while rotating at 37 °C. CUBIC-L solution was refreshed on day 3 and on the final day samples were washed 5× with PBS. Skulls were decalcified over 5 d in CUBIC-B solution (10 wt% EDTA (Boston BioProducts) and 15 wt% imidazole (Tokyo Chemical Industry, catalog no. 1352)). Primary antibody staining using chicken anti-GFP (Abcam, ab13790, 1:300) was performed in staining buffer comprising PBS with 1% Triton X-100 (Sigma-Aldrich), 10% normal goat serum (Vector Labs) and 0.2% sodium azide (Sigma-Aldrich) for 4 d while gently shaking (200 r.p.m.) at room temperature. Samples were then washed with CUBIC wash buffer (PBS with 1% Triton X-100), after which samples were incubated in goat anti-chicken AF555 (Thermo Fisher Scientific, catalog no. A-21437) secondary antibody. This staining was performed in the same buffer used for the primary antibody incubation step at room temperature for 3 d. Samples were subjected to refractive index matching in CUBIC-R (45 wt% antipyrine (Tokyo Chemical Industry, catalog no. 0640), 30 wt% nicotinamide (Tokyo Chemical Industry, catalog no.0855)) for 2 d at room temperature, after which samples were ready for whole-mount confocal imaging.

Bioluminescence imaging. Studies utilizing *S. pneumoniae* Xen10 followed the intracisternal injection technique described above. Briefly, 5×10^3 *S. pneumoniae* Xen10 or an equivalent volume of aCSF was injected into age-matched mice for imaging at 12, 36 and 48 h after injection. Images were acquired with an AmiX BLI/X-Ray Scanner (AmiX) using medium binning and a 3-min exposure time. Photon intensity was scaled at a range of 4×10^4–2×10^7 photons cm^{-2} to allow for crossgroup comparisons. The signal was quantified with AMIView software by defining a region of interest across the head, neck and spine. This region of interest was then uniformly fitted to each individual mouse.

Bacterial colony-forming unit assay. Colony-forming unit assays from blood and CSF of sham and meningitis mice were performed 48 h after injection. Mice were fixed on to a stereotactic frame in a manner similar to the orientation used for intracisternal injections. To sample the CSF, the injection site was reopened and the dura mater punctured with a glass micropipette to aspirate 5–10 µl of CSF. Mice were then removed from the frame and 100 µl of blood was collected by cardiac puncture. For colony-forming units of skull and tibia, bones were aseptically harvested from the sham and meningitis groups, and the meninges were dissected from the skull in sterile PBS containing 5% bovine serum albumin (BSA) and 2 mM EDTA. Pilot experiments were performed to titer dilutions of CSF, blood, skull or tibia homogenate necessary to visualize bacterial growth on blood agar plates containing 50 µg ml^{-1} of kanamycin (TEKnova, catalog nol. T0194). A cell spreader was used to evenly distribute homogenates across the plate and the plate was stored at 37 °C for 24 h before analysis. Plates were photographed and colonies quantified for relative comparisons.

***S. pneumoniae* detection by qPCR.** We analyzed relative amounts of the *S. pneumoniae* gene *psaA* from tibias and skulls excised from the sham and meningitis cohorts of adult mice 48 h after intracisternal injection of aCSF or *S. pneumoniae* Xen10. Injections were performed as described above and bones were aseptically excised from mice. All mice were perfused with 20 ml of PBS before removal of the tibia and skull bones. After the bones had been excised, the meninges were dissected from the skull bone, after which the tibia and skull bones were snap-frozen in liquid nitrogen and stored at −80 °C overnight before subsequent analysis. DNA isolation protocol and primers used to detect *S. pneumoniae psaA* were adapted from an established protocol[42]. Briefly, three primers were custom synthesized (IDT): *psaA* forward (5′-GCCCTAATAAATTGGAGGATCTAATGA-3′), *psaA* reverse (5′-GACCAGAAGTTGTATCTTTTTTTCCG-3′) and *psaA* probe (5′-HEX-CTAGCACATGCTACAAGAATGATTGCAGAAAGAAA-3′-phosphate) for qPCR-based relative expression analysis. Skull and tibia bones were trimmed to 50 mg and homogenized in 180 µl of ALT buffer containing 0.04 g ml^{-1} of lysozyme (Sigma-Aldrich) and 75 U ml^{-1} of mutanolysin (Sigma-Aldrich). Digestion was performed for 1 h at 37 °C in a shaking water bath. DNA isolation and purification were performed following the manufacturer's guidelines from the QIAGEN DNA Mini-Kit manual. The genomic DNA for each sample was spectrophotometrically measured (Thermo Fisher Scientific, NanoDrop 2000) and equivalent DNA amounts were loaded for subsequent qPCR. Reactions were allowed to run for 45 thermal cycles for amplification in duplicate. Cycle threshold values >40 were considered negative.

Flow cytometry. To assess meningeal, blood, skull and tibia bone marrow hematopoietic cells, mice were anesthetized, sacrificed and perfused with 20 ml of PBS to remove blood. Tibia and skull were excised, and then the meninges were removed from the skull and mechanically homogenized in buffer (PBS with 5% BSA and 2 mM EDTA). Homogenate was filtered through a 40-µm strainer, centrifuged for 5 min at 340*g* and resuspended in FACS buffer (PBS with 0.5% BSA) for antibody staining[25]. To analyze HSPCs, we followed previously established gating strategies[19,43–45]. Cells were first stained with biotin-conjugated, anti-mouse antibodies (all used at 1:100 dilution) against CD3 (BioLegend, clone 145-2C11), CD4 (BioLegend, clone GK1.5), CD8a (BioLegend, clone 53-6.7), CD49b (BioLegend, clone DX5), CD90.2 (BioLegend, clone 30-H12), CD19 (BioLegend, clone 6D5), B220 (BioLegend, clone RA3-6B2), NK1.1 (BioLegend, clone PK136), TER119 (BioLegend, clone TER-119), CD11b (BioLegend, clone M1/70), CD11c (BioLegend, clone N418) and Gr1 (BioLegend, clone RB6-8C5, all diluted 1:300), which all served as lineage (Lin) markers and LIVE/DEAD Fixable Aqua Dead Cell Stain (Life Technologies, 1:100). Staining was done for 30 min on ice followed by a wash/spin and resuspension in FACS buffer for secondary staining (all at 1:100). LSK analysis was performed by staining cells with ckit-PE-Cy7 (BioLegend, clone 2B8), Sca1-BV605 (BioLegend, clone D7) and Streptavidin-APC-Cy7 (BioLegend, 1:100). LSKs were identified as Lin$^-$c-kit$^+$Sca1$^+$. For CMP analysis, cells were stained with CD34 (vendor, clone, dilution, catalog number; BD, RAM34, 1:100, 553733) and CD16/32 (BioLegend, 93, 1:100, 101337). Antibodies listed in the secondary staining panel were used at 1:100 dilution in a 500-µl single-cell suspension volume for 30 min on ice. Cells were further stained with the APC BrdU Flow Kit (BD Biosciences, catalog no. 552598) following the manufacturer's guidelines for analysis. BrdU was administered via intraperitoneal injection 3 h before sacrifice to analyze LSK proliferation 6 h after intracisternal bacteria injection. Cells were then washed with FACS buffer, spun down at 340*g* for 5 min and resuspended in 400 µl of buffer for analysis. Events were recorded on an LSRII flow cytometer and accompanying FACS DIVA 6.1 software (BD Biosciences). Data were analyzed with FlowJo 10 software (Becton Dickinson). For tibia and skull leukocyte analysis, a similar sample preparation to the above was utilized, but cells were stained with the following antibodies at 1:100, unless otherwise noted: anti-CD19–PE/Cy7 (6D5, 1:50, BioLegend), anti-CD3–PE (BioLegend, 17A2, 1:50), anti-CD45–AF700 (BioLegend, 30-F11), anti-Ly6C–BV605 (HK1.4, BioLegend), anti-Ly6G–FITC (Biolegend, 1A8), anti-CD11b–APC (BioLegend, M1/70) and anti-CD115–BV421 (BioLegend, AFS98). For meningeal flow cytometry, meninges were mechanically digested followed by digestion in enzymatic buffer for 30 min containing PBS with 2.5 mg ml^{-1} of Collagenase D (Sigma-Aldrich) and 0.1 mg ml^{-1} of DNase I (Sigma-Aldrich). Meninges were then filtered, spun down and prepared for staining with the antibody panels described above. For chimerism experiments, blood was obtained via retro-orbital bleeding using 50-µl heparinzed capillary tubes (BD) and subject to red blood cell lysis (Sigma-Aldrich) for 10 min at room temperature. After this, cells were washed with FACS buffer and prepared for staining in parallel with the meninges. Chimerism-related flow cytometry was accomplished using the following antibodies: CD45.1 (vendor, clone, dilution, catalog number; BioLegend, A20, 1:100, 110716), CD45.2 (BioLegend, 104,1:100, 109832), CD11b (BioLegend, M1/70, 1:100, 101212), CD115 (BioLegend, AFS98, 1:100, 135517), Ly6G (BioLegend, 1A8, 1:100, 127617).

LSK sorting and transfer. Two tibias and two femurs were excised and the bone marrow aspirated with a 25G needle into a syringe containing FACS buffer, followed by centrifugation and resuspension for staining. Immunostaining of LSKs for cell sorting was done as described above for LSK quantification across the sham and meningitis groups with minor changes. After staining, the cell pellet was spun down and resuspended in FACS buffer for lineage cell depletion using the Direct Lineage Cell Depletion Kit (Miltenyi Biotec, catalog no. 130-110-470) following the manufacturer's instructions. After depletion, cells were centrifuged and resuspended for cell sorting; 40,000 LSKs were sorted per individual C57/Bl6 or *Myd88*$^{-/-}$ (Jackson Lab, catalog no. 009088) donor mouse. LSKs were sorted into FACS buffer and stained with either Dil Cell-Labeling Solution for *Myd88*$^{-/-}$ LSKs (Thermo Fisher Scientific, catalog no. V22885) or DiD Cell-Labeling Solution for WT LSKs (Thermo Fisher Scientific, catalog no. V22887) per manufacturer's instructions. The 40,000 LSKs per donor genotype were mixed and injected simultaneously via the tail vein and allowed to home/settle for 3 d. On day 3, recipient mice underwent intracisternal injection of bacteria as described above, followed by intravital imaging 2 d later.

For skull-specific bone marrow transplantation, anesthetized C57/Bl6 CD45.2 wild-type mice were immobilized on lucite platforms between two 3.9-cm thick lead slabs with 2-cm diameter apertures[46] to expose the head to two doses of 6-Gy irradiation. Mice then received 4×10^6 CD45.1 bone marrow cells and were used for experiments 4 weeks later[11].

Flow cytometric detection of bacteria. Mice were IC injected with GFP + *S. pneumoniae* as described above and analyzed 48 h after injection. Skulls were aseptically excised followed by meningeal dissection under a light microscope. Samples were mechanically homogenized in buffer (PBS with 5% BSA and 2 mM EDTA), filtered through a 40-µm strainer and spun down for 5 min at 340*g*. Supernatant containing bacteria was isolated and further spun at 5,000*g*

for 10 min and resuspended in 400 µl to analyze free-floating bacteria. Cell pellets were stained with CD45-AF700 (BioLegend, clone 30F11, 1:100) in FACS buffer on ice for 30 min. Samples were washed with 2 ml of FACS buffer, spun down at 340*g* for 5 min and resuspended in FACS buffer for analysis. Events were recorded on an LSRII flow cytometer and accompanying FACS DIVA 6.1 software (BD Biosciences). Data were analyzed with FlowJo 10 software (Becton Dickinson). Cells were gated for single cells by forward scatter and side scatter parameters, as previously described, and leukocytes were defined as $CD45^+$ cells.

RNA extraction and qPCR. RNA was isolated from the meninges using the RNeasy Micro kit (QIAGEN). High-Capacity RNA to cDNA kit (Applied Biosystems) was used for first-strand complementary DNA synthesis from meningeal RNA. TaqMan gene expression kits were utilized to measure target genes of interest: *Il-1β* (catalog no. Mm00434228_m1, Thermo Fisher Scientific), *Il-6* (catalog no. Mm00446190_m1, Thermo Fisher Scientific) and *TNF-α* (catalog no. Mm00443258_m1, Thermo Fisher Scientific). Target gene primers were all FAM-MGB and all target gene relative expression analyses were normalized to a housekeeping gene, *Gapdh* (VIC-MGB, Mm99999915_g1, Thermo Fisher Scientific). Samples were run on a 7500 Real-Time PCR machine (Applied Biosystems).

Image analysis. Images were processed and analyzed using FIJI v.2.1.0, MATLAB R2015b (Mathworks) or Volocity 3D imaging software v.6.3 (Perkin Elmer). To complete ex vivo 2-photon microcopy channel analysis for CSF tracer presence, *z*-stacks were untilted using MATLAB (2020b) such that the skull surface spanned the least number of *z* depths, that is, it lay approximately flat. Afterwards, enhanced contrast was performed on each channel (R, G, B) to correct for intensity attenuation due to light absorption in the tissue. For confocal images, *z*-stacks of 0.75, 1.0 or 2.0 µm per slice were taken depending on the imaging objective (×4, ×10 or ×20). These conditions were consistent across all single-photon confocal microscopy images in both ex vivo imaging and IVM experiments. Images were 3D max-intensity or sum-intensity projected using FIJI and background subtracted, followed by an automated protocol to remove speckle-based noise. Manual thresholding and contrast adjustment were applied uniformly across all samples. To ensure processing step uniformity, FIJI macros were recorded for the first image processed and then applied to all images from the same cohort. Where indicated, certain images were further analyzed using Volocity software for preparing 3D surface reconstructions. The 3D rendering was automatically generated and the image contrast, density and brightness were uniformly set across all images analyzed. Movies were generated in Volocity using snapshots of post-processed datasets and then incorporated into a single video in AVI format.

Statistical information. All statistical analyses were performed using GraphPad Prism (GraphPad Software v.10). All quantitative results are reported as the mean ± s.d. For single variable comparisons of parametric datasets for two groups, an unpaired Student's *t*-test was performed. For nonparametric datasets of unpaired data, a Mann–Whitney test was performed. For parametric datasets for multiple groups, a one-way analysis of variance (ANOVA) was performed with a post-hoc correction for multiple comparisons as indicated in individual legends. For nonparametric datasets for multiple groups, a Kruskal–Wallis test was performed, followed by post-hoc correction for multiple comparisons where indicated. For all statistical tests, a P value <0.05 was considered significant. No statistical methods were used to predetermine sample sizes but our sample sizes are in agreement with those reported in previous publications[8,19,43]. Animals were not excluded from experimental data analysis, with the exception of two mice that died before the experimental timepoint (6 h and 24 h), caused by a failed intracisternal magna injection. Due to the preparation of groups necessary for intracisternal injections and subsequent nature of the data acquisition of these experiments, it was possible to perform these experiments only in a semi-blinded fashion. As tissue harvesting and preparation required two to three people, only one person was made aware of the control versus experimental groupings, with the remaining experiment members blinded. Cell sorting of LSKs was also done in a blinded fashion (for example, wild-type versus *Myd88* knockout) by staff scientists at our flow cytometry core. Animals were randomly assigned to control or experimental groups.

Reporting Summary. Further information on research design is available in the Nature Research Reporting Summary linked to this article.

Data availability

The authors will make any source data within the manuscript available upon reasonable request. The large file sizes accompanying the extensive imaging data used can be provided along with relevant accessibility information for software packages associated with each file. Requests may be sent to any of the corresponding authors. Email addresses: charles_lin@hms.harvard.edu, moskowitz@helix.mgh.harvard.edu, mnahrendorf@mgh.harvard.edu.

References

39. Kjos, M. et al. Bright fluorescent *Streptococcus pneumoniae* for live-cell imaging of host–pathogen interactions. *J. Bacteriol.* **197**, 807–818 (2015).
40. Xu, C. et al. Stem cell factor is selectively secreted by arterial endothelial cells in bone marrow. *Nat. Commun.* **9**, 2449 (2018).
41. Mestre, H., Mori, Y. & Nedergaard, M. The brain's glymphatic system: current controversies. *Trends Neurosci.* **43**, 458–466 (2020).
42. Carvalho Mda, G. et al. Evaluation and improvement of real-time PCR assays targeting *lytA*, *ply*, and *psaA* genes for detection of pneumococcal DNA. *J. Clin. Microbiol.* **45**, 2460–2466 (2007).
43. Dutta, P. et al. Myocardial infarction activates $CCR2^+$ hematopoietic stem and progenitor cells. *Cell Stem Cell* **16**, 477–487 (2015).
44. Kiel, M. J. et al. SLAM family receptors distinguish hematopoietic stem and progenitor cells and reveal endothelial niches for stem cells. *Cell* **121**, 1109–1121 (2005).
45. Rodriguez-Fraticelli, A. E. et al. Clonal analysis of lineage fate in native haematopoiesis. *Nature* **553**, 212–216 (2018).
46. Miller, M. A. et al. Radiation therapy primes tumors for nanotherapeutic delivery via macrophage-mediated vascular bursts. *Sci. Transl. Med.* **9**, eaal0225 (2017).

Acknowledgements

We thank J.-W. Veening for providing fluorescent bacteria and K. Joyes for editing the manuscript. This work was funded in part by US federal funds from the National Institutes of Health (grant nos. HL158040, HL142494, HL139598, HL125428, NS108419 and HL135752), the Global Research Lab program (grant no. NRF-2015K1A1A2028228) and the National Priority Research Center program (grant no. NRF-2021R1A6A1A03038865) of the Korean Research Foundation. M.H. was supported by an American Heart Association Career Development Award (no. 19CDA34490005).

Author contributions

F.E.P. conceived the study, designed, performed and analyzed imaging and wet lab experiments, induced meningitis, interpreted data and created the figures. J.C.C.-H. designed, performed and analyzed imaging experiments. C.Y. and Z.K. optimized the meningitis model for imaging assays, performed and analyzed experiments, interpreted data and discussed strategy. A.P., M.H., N.M., G.W., D.C., M.Y, J.G., M.J.S. and D. Rohde performed experiments and collected data. C.V. participated in optical clearing and imaging experiments. D. Richter and J.W.W. provided image analysis. D.B., C.V., D.E.K., F.K.S. and R.W. discussed data and experimental design. F.E.P. and M.N. wrote the manuscript with input from all authors. C.L., M.A.M. and M.N. conceived and directed the study.

Competing interests

M.N. has received funds or material research support from Lilly, Alnylam, Biotronik, CSL Behring, GlycoMimetics, GSK, Medtronic, Novartis and Pfizer, as well as consulting fees from Biogen, Gimv, IFM Therapeutics, Molecular Imaging, Sigilon, NovoNordisk and Verseau Therapeutics. The other authors declare no competing interests.

Additional information

Extended data are available for this paper at https://doi.org/10.1038/s41593-022-01060-2.

Supplementary information The online version contains supplementary material available at https://doi.org/10.1038/s41593-022-01060-2.

Correspondence and requests for materials should be addressed to Charles P. Lin, Michael A. Moskowitz or Matthias Nahrendorf.

Peer review information *Nature Neuroscience* thanks Sandrine Bourdoulous, Michal Schwartz, Hiroki Ueda, and the other, anonymous, reviewer(s) for their contribution to the peer review of this work.

Reprints and permissions information is available at www.nature.com/reprints.

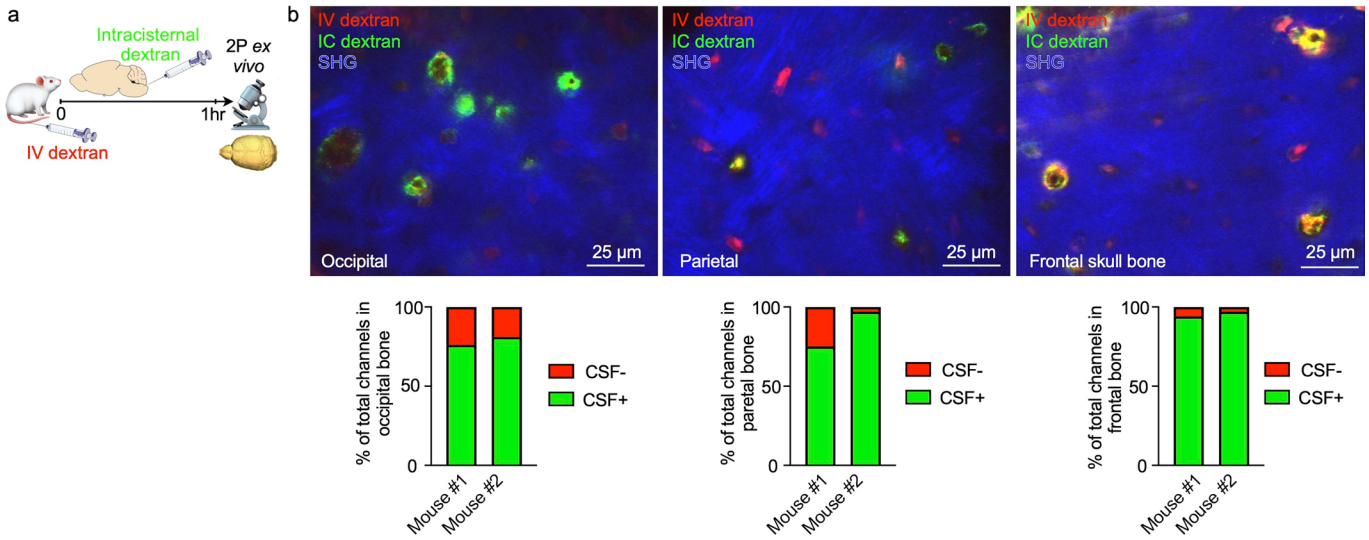

Extended Data Fig. 1 | CSF tracer outflow in occipital, parietal and frontal skull bones. a, Experimental outline. Ex-vivo z-stack (54 µm stack at 1 µm/step) of occipital, parietal and frontal skull cortex after IC and IV injection of fluorescently labeled dextran. Bone is visualized by second harmonic generation around channels **b**, Imaging of CSF tracer outflow through channels in different skull bones, assessed in n=2 mice. Bar graphs depict the proportion of skull channels that were positive for CSF tracer.

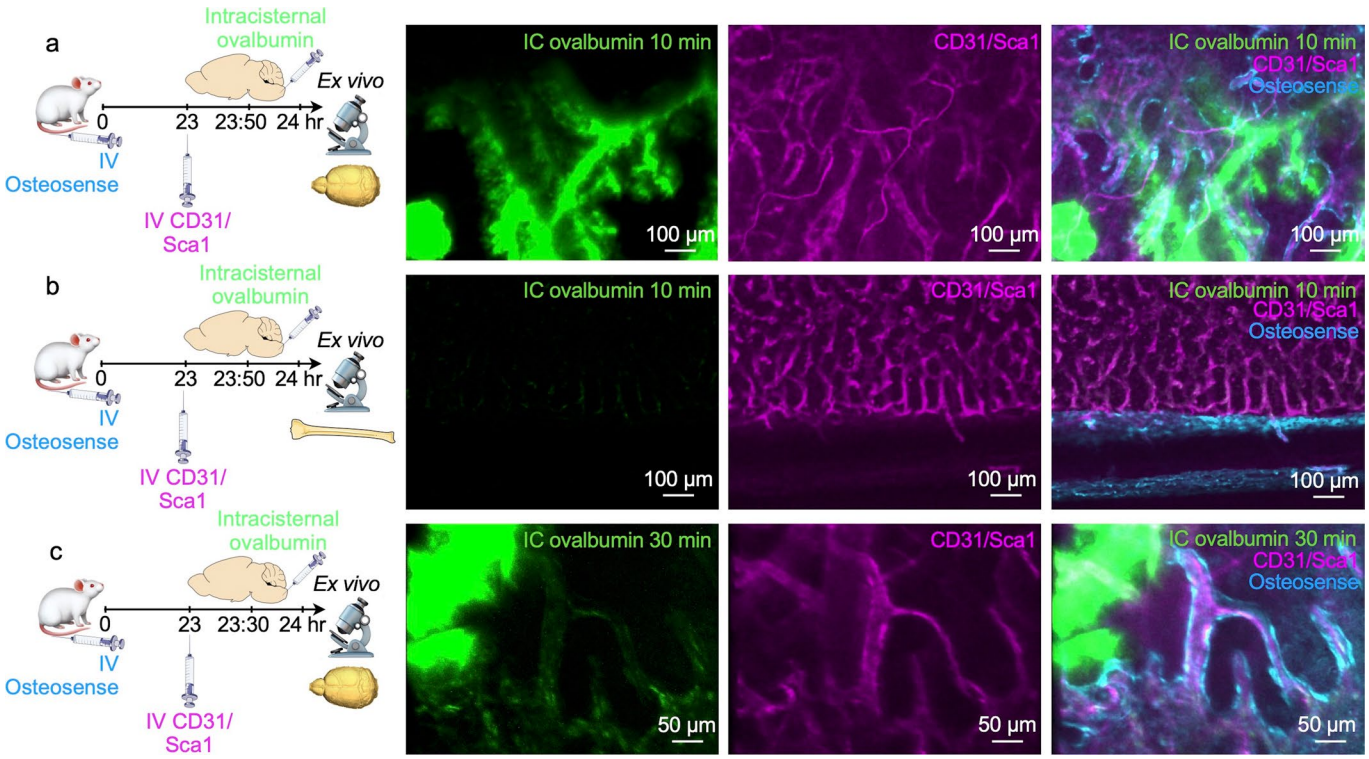

Extended Data Fig. 2 | Dynamics of CSF outflow into bone marrow. a, *Ex vivo* imaging of whole-mount skull 10 min after intracisternal (IC) injection of ovalbumin. Intravenous(IV) injection of CD31/Sca1 labeled vasculature and IV osteosense the bone. **b**, *Ex vivo* imaging of tibia 10 minutes after intracisternal injection of ovalbumin. **c**, Imaging 30 minutes after intracisternal injection of ovalbumin. Data is representative of 2 independent experiments.

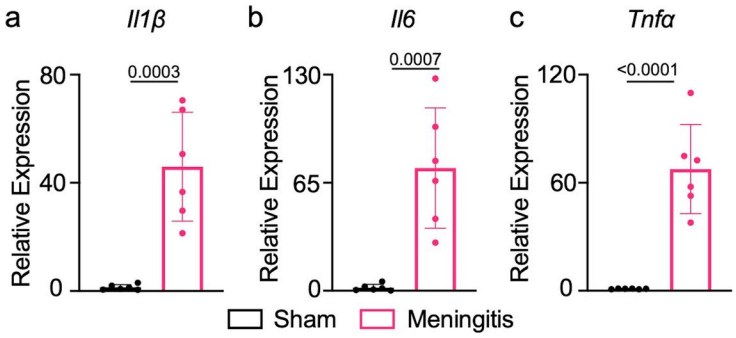

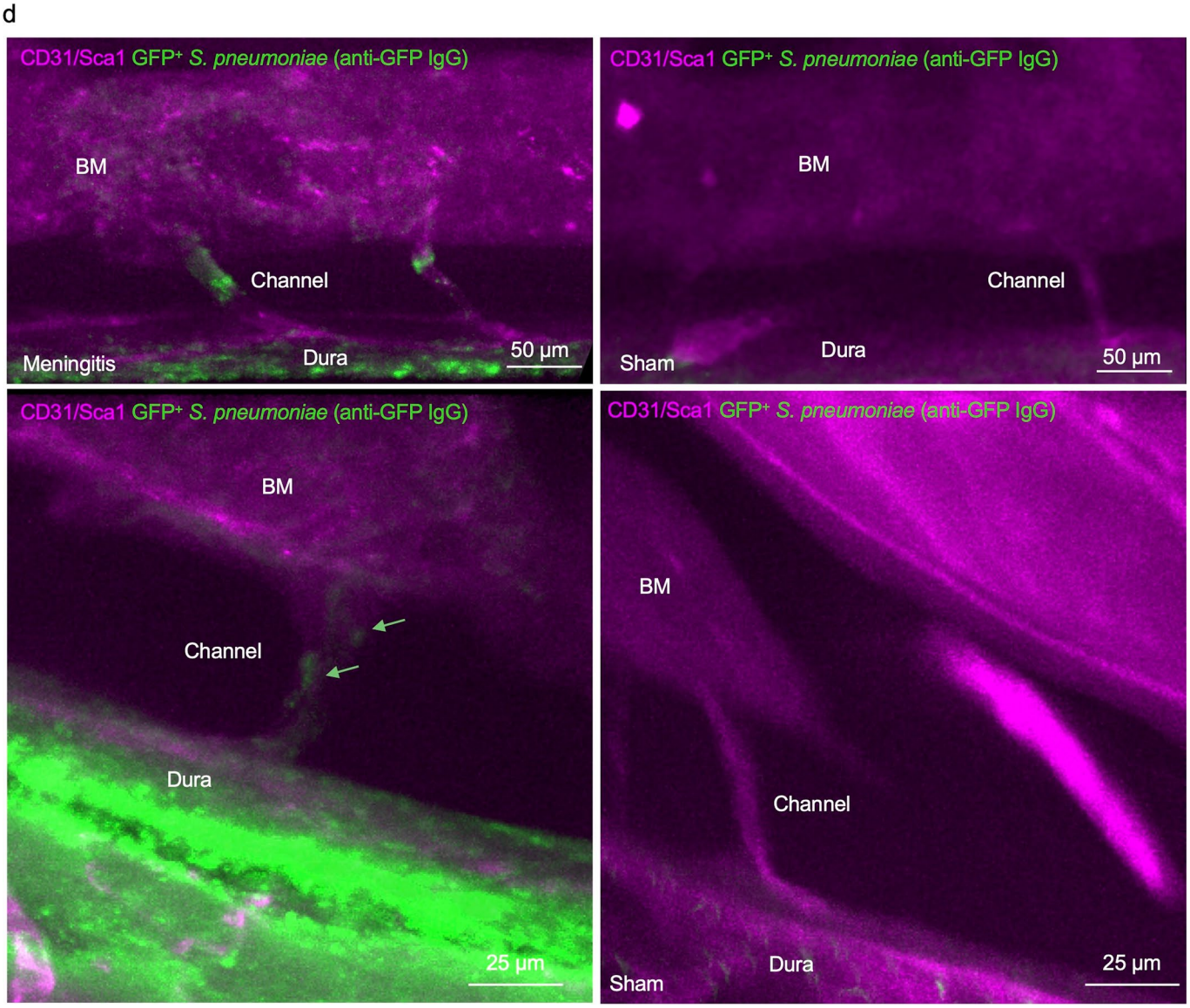

Extended Data Fig. 3 | Inflammation in the meninges driven by bacterial meningitis. qPCR analysis of meninges isolated from either sham controls that were intracisternally injected with artificial CSF or mice 48 hours after intracisternal infection for relative expression analysis of **a**, *Il1β*, **b**, *Il6* and **c**, *Tnfα* (mean ± SD; n=6 mice per group; *P* values represent an unpaired two-tailed t-test from a single experiment). **d**, Raw images obtained by whole mount *ex vivo* imaging of the skull 48 hours after intracranial sham or *S. pneumoniae* injection. First representative image is the original data from Fig. 5b while the second set represents additional examples of channel morphology and bacterial propagation. Green arrow highlights bacteria (scale: 50 and 25 μm).

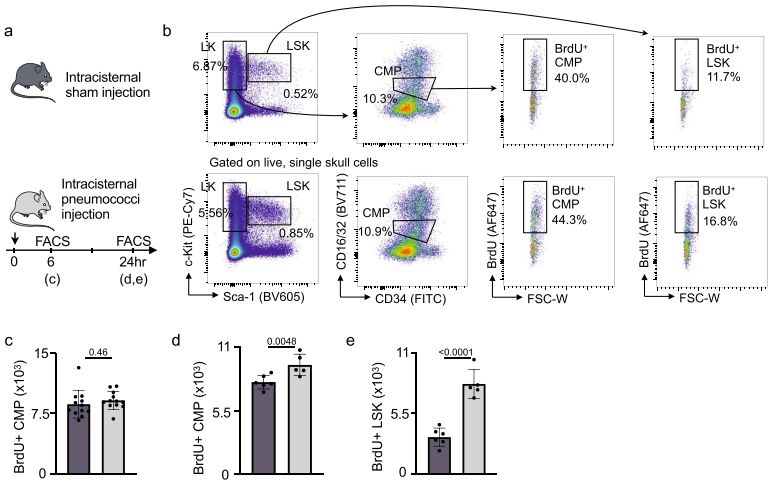

Extended Data Fig. 4 | Analysis of skull hematopoietic progenitors during meningitis. a, Experimental outline for calvarial hematopoietic progenitor analysis. **b**, Flow cytometry gating. **c**, Quantitation of calvarial BrdU$^+$ common myeloid progenitors (CMP) 6 hours after intracisternal sham or *S. pneumococci* injection. (n=11 sham and 12 meningitis, *P* value represents an unpaired, two-tailed t-test). **d**, Quantitation of calvarial BrdU$^+$ CMP 24 hours after intracisternal sham or *S. pneumococci* injection. (n=6 mice per group, *P* value represents an unpaired, two-tailed t-test) **e**, Quantitation of calvarial BrdU$^+$ LSK 24 hours after intracisternal sham or *S. pneumococci* injection. (n=6 mice per group, *P* value represents an unpaired, two-tailed t-test).

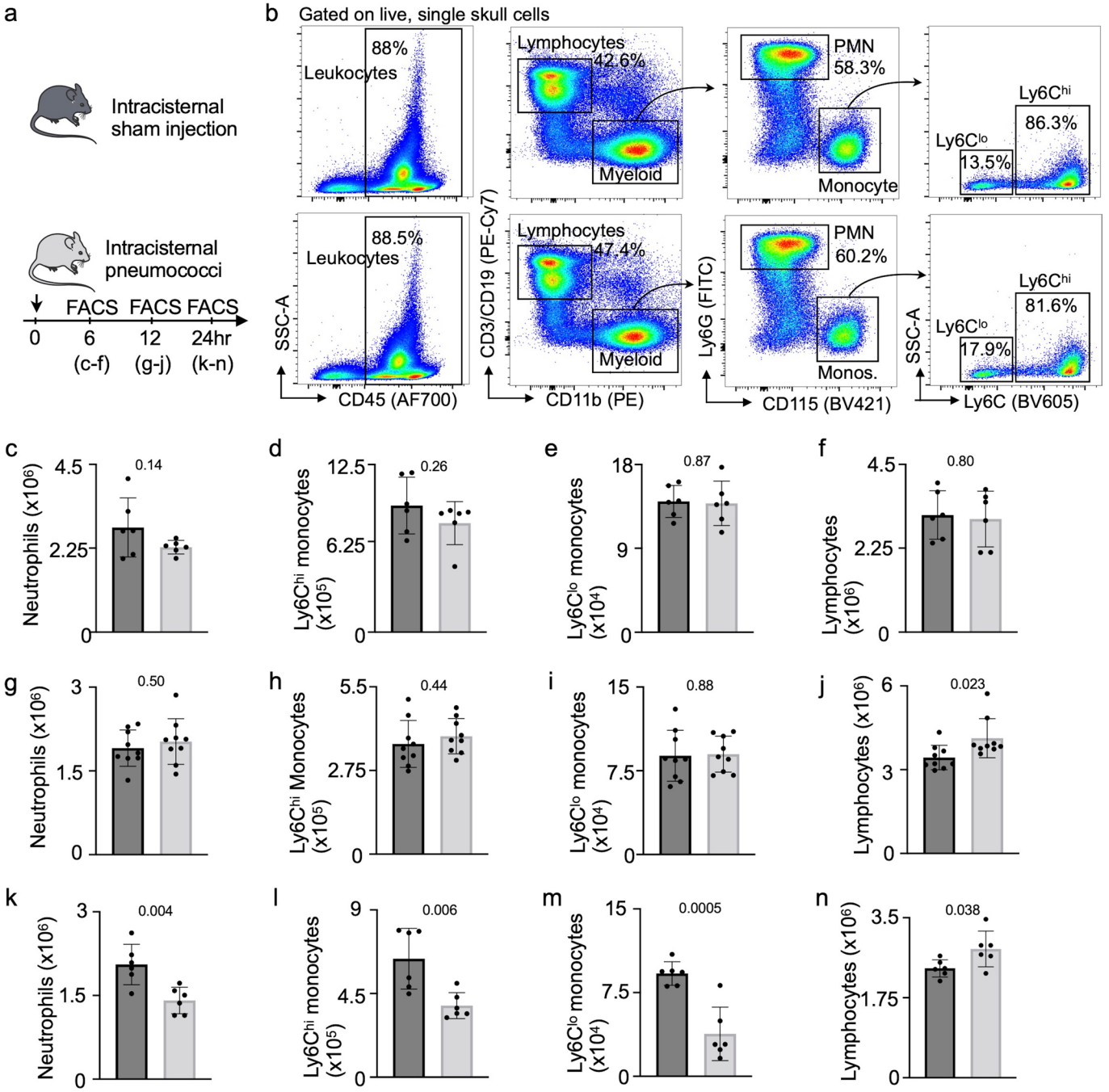

Extended Data Fig. 5 | Analysis of calvarial leukocytes during meningitis. a, Experimental outline of calvarial leukocyte analysis. **b**, Flow cytometry gating. **c-f**, Quantitation of calvarial leukocytes 6 hours after intracisternal *S. pneumococci* injection shows neutrophils, monocyte subsets and total lymphocytes (n=5 mice per group). **g-j**, Quantitation of calvarial leukocytes 12 hours after *S. pneumococci* injection including neutrophils (g), Ly6C^{hi} monocytes (h), Ly6C^{lo} monocytes (i) and total lymphocytes (j) (n=9 sham and 8 meningitis). **k-n**, Quantitation of calvarial leukocytes 24 hours after *S. pneumococci* injection including neutrophils (k), Ly6C^{hi} monocytes (l), Ly6C^{lo} monocytes (m) and total lymphocytes (n) (n=6 mice per group). (*P* values represent unpaired, two-tailed t-tests, data are mean values ± SD).

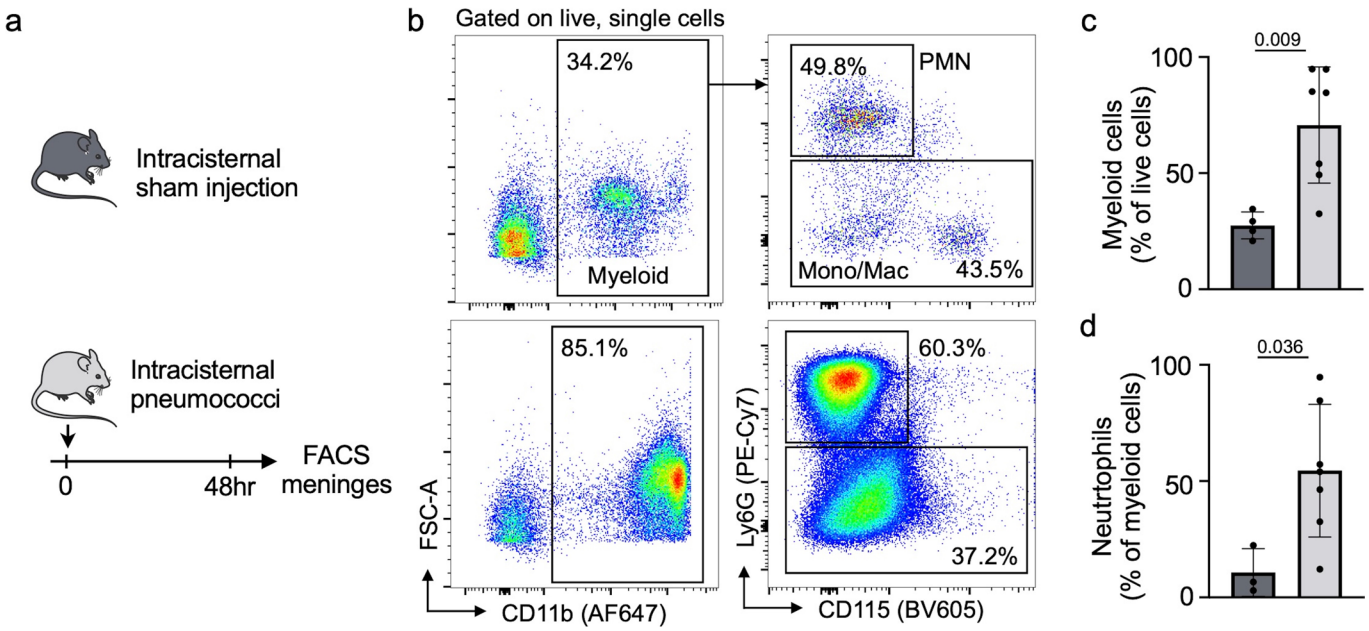

Extended Data Fig. 6 | Meningeal leukocytes expand in bacterial meningitis. a, Experimental outline. **b**, flow cytometry plots of control meninges (upper panel) and meninges 48 hours after infection. **c**, quantification of CD11b$^+$ myeloid cells and **d**, Ly6G$^+$ neutrophils in meninges (n=4 sham and 7 meningitis mice, *P* values represent unpaired, two-sided t tests, data are mean values ± SD).

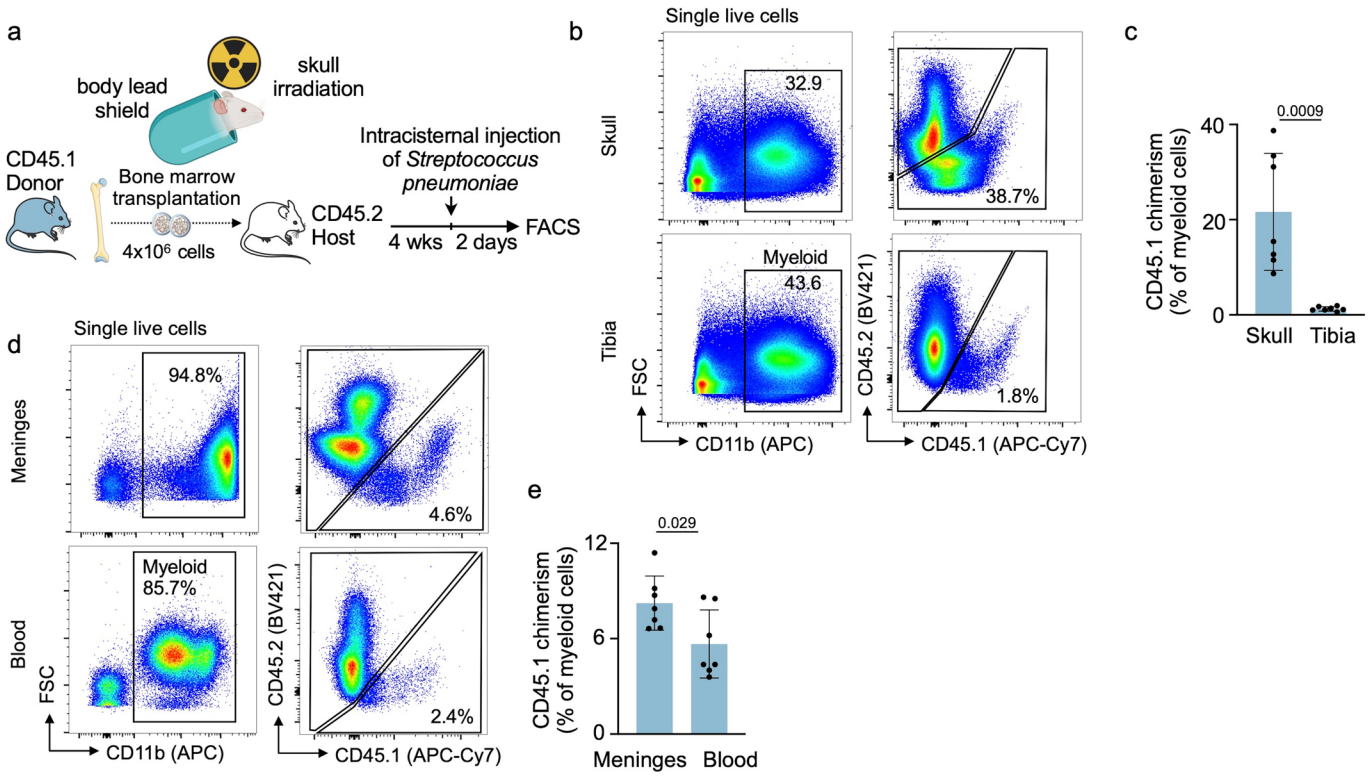

Extended Data Fig. 7 | Tracking of skull leukocytes to infected meninges. a, Experimental outline indicating skull marrow transplantation, followed by induction of meningitis 4 weeks later. **b**, flow plots and (**c**) quantitation of myeloid cell chimerism in irradiated skull versus lead-shielded tibia 4 weeks after transplantation (n=7 recipient mice, *P* value represents unpaired, two-tailed t test, data are mean values ± SD). **d**, flow plots and (**e**) quantification of myeloid cell chimerism in the meninges and in blood (n=7 recipient mice, *P* value represents unpaired, two-tailed t tests, data are mean values ± SD).

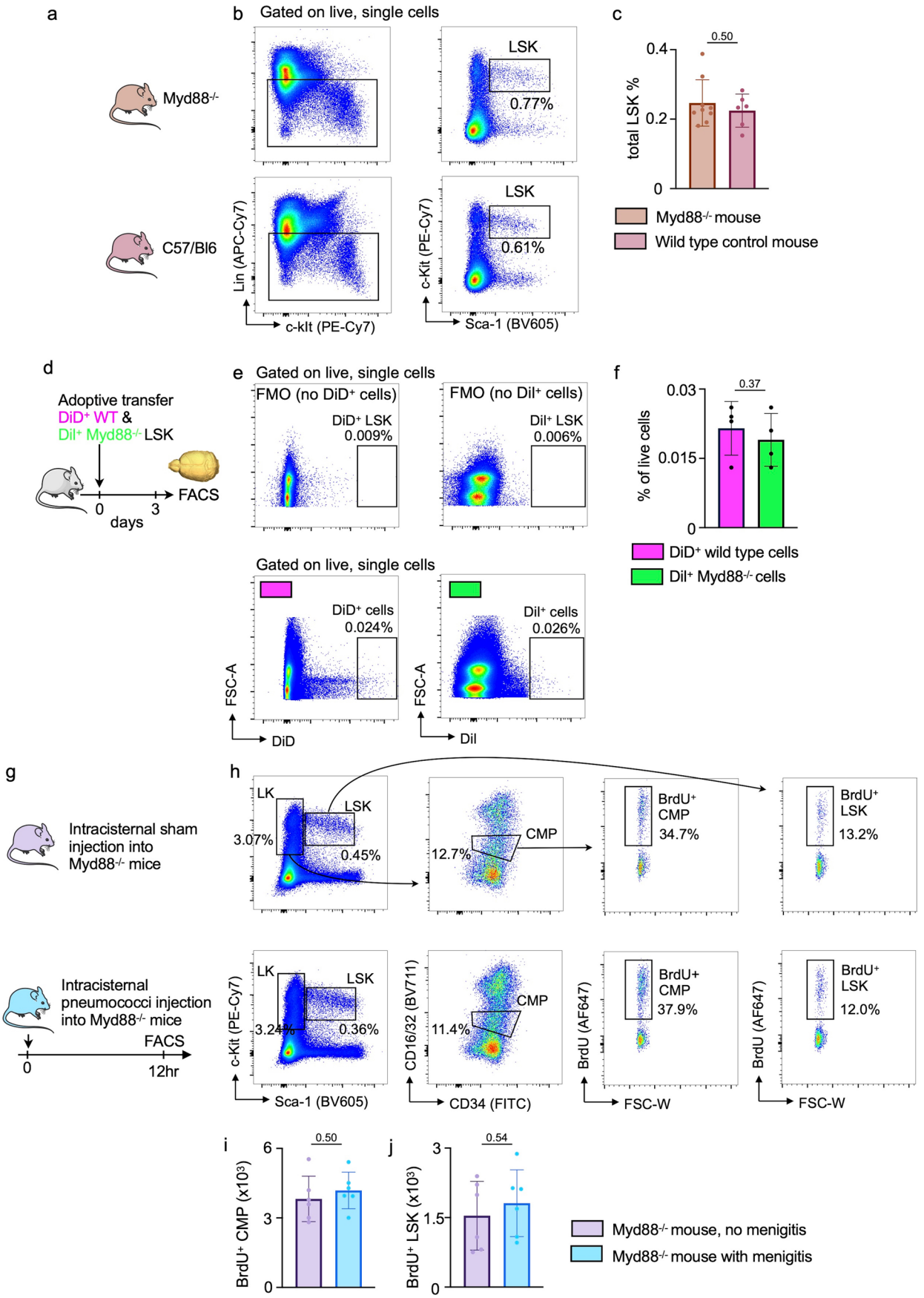

Extended Data Fig. 8 | See next page for caption.

Extended Data Fig. 8 | Myd88-related sensing in the skull marrow. a, Experimental groups include wild type and Myd88$^{-/-}$ mice. The skull marrow was assessed by flow cytometric staining for lineage markers Sca-1 and c-kit. **b**, Flow cytometry plots and **c**, quantitation of LSK % as a total of all live lineage negative single cells in the calvarial marrow of steady-state Myd88$^{-/-}$ or wild-type C57/Bl6 mice (n=9 sham and 6 meningitis mice, *P* value represents an unpaired, two-tailed t-test, data are mean values ± SD). **d**, Experimental outline. Non-irradiated wild type recipient mice received a mix of 40,000 LSK from wild type donors (labeled with the membrane dye DiD) and from Myd88-/- donors (labeled with DiI). **e**, Flow cytometry gating and **f**, analysis of the skull bone marrow 3 days later showed a similar seeding of LSK irrespective of phenotype (n=4 mice per group, unpaired, two-tailed t-test). **g**, Experimental outline of calvarial progenitor analysis in Myd88$^{-/-}$ mice with and without meningitis. **h**, Flow cytometry gating. **i**, Quantitation of calvarial BrdU^{+} CMP 12 hours after intracisternal sham or *S. pneumococci* injection. (n=11 sham and 12 meningitis mice per group, unpaired two-tailed t-test, data are mean values ± SD). **j**, Quantitation of calvarial BrdU^{+} LSK 24 hours after intracisternal sham or *S. pneumococci* injection. (n=6 mice group, unpaired two-tailed t-test, data are mean values ± SD).

nature portfolio

Corresponding author(s): Matthias Nahrendorf

Last updated by author(s): Mar 18, 2022

Reporting Summary

Nature Portfolio wishes to improve the reproducibility of the work that we publish. This form provides structure for consistency and transparency in reporting. For further information on Nature Portfolio policies, see our Editorial Policies and the Editorial Policy Checklist.

Statistics

For all statistical analyses, confirm that the following items are present in the figure legend, table legend, main text, or Methods section.

n/a	Confirmed	
☐	☒	The exact sample size (*n*) for each experimental group/condition, given as a discrete number and unit of measurement
☐	☒	A statement on whether measurements were taken from distinct samples or whether the same sample was measured repeatedly
☐	☒	The statistical test(s) used AND whether they are one- or two-sided *Only common tests should be described solely by name; describe more complex techniques in the Methods section.*
☐	☒	A description of all covariates tested
☐	☒	A description of any assumptions or corrections, such as tests of normality and adjustment for multiple comparisons
☐	☒	A full description of the statistical parameters including central tendency (e.g. means) or other basic estimates (e.g. regression coefficient) AND variation (e.g. standard deviation) or associated estimates of uncertainty (e.g. confidence intervals)
☐	☒	For null hypothesis testing, the test statistic (e.g. *F*, *t*, *r*) with confidence intervals, effect sizes, degrees of freedom and *P* value noted *Give P values as exact values whenever suitable.*
☒	☐	For Bayesian analysis, information on the choice of priors and Markov chain Monte Carlo settings
☒	☐	For hierarchical and complex designs, identification of the appropriate level for tests and full reporting of outcomes
☒	☐	Estimates of effect sizes (e.g. Cohen's *d*, Pearson's *r*), indicating how they were calculated

Our web collection on statistics for biologists contains articles on many of the points above.

Software and code

Policy information about availability of computer code

Data collection	Flow cytometry data were acquired on an LSRII flow cytometer running FACS DIVA 6.1 software for event acquisition. For LSK cell-sorting, a BD FACs Aria running FACS DIVA 6.1 (BD Biosciences) was used by a staff scientist at the Harvard Stem Cell Institute and Center for Regenerative Medicine Flow Core. qPCR was performed on a Bio-Rad CFX96 Real Time PCR Machine. Single photon confocal microscopy was performed on an Olympus IV100 microscope equipped with IV10-ASW 01.01.00.05 software (Olympus). 2-photon microscopy was performed on a custom-built two-photon excitation microscope equipped with a Ti: Sapphire laser oscillator (Spectra-Physics InSight X3) and coupled with Olympus 60x water-immersion objective lens. Laser scanning and acquisition were controlled by custom-built software.
Data analysis	Flow data was analyzed with FlowJo 10 software (BD Biosciences). Quantitative analysis of flow data and qPCR data was organized on Microsoft Excel and exported onto GraphPad Prism 10 software (GraphPad). Confocal and 2-photon microscopy data was analyzed on FIJI open-source software v2.1. 3-D reconsructions were generated using Volocity software version 6.3 (PerkinElmer). 2-PM image data was analyzed with MATLAB v2020b code to construct z-stacks and Amira v5.3.2 software was used for microCT data analysis.

For manuscripts utilizing custom algorithms or software that are central to the research but not yet described in published literature, software must be made available to editors and reviewers. We strongly encourage code deposition in a community repository (e.g. GitHub). See the Nature Portfolio guidelines for submitting code & software for further information.

Data

Policy information about availability of data

All manuscripts must include a data availability statement. This statement should provide the following information, where applicable:

- Accession codes, unique identifiers, or web links for publicly available datasets
- A description of any restrictions on data availability
- For clinical datasets or third party data, please ensure that the statement adheres to our policy

All raw data can be made available upon reasonable request and a statement in the manuscript reflects the availability status of our collective data. The authors will make any source data within the manuscript available upon reasonable request. The large file sizes accompanying the extensive imaging data used can be provided along with relevant accessibility information for software packages associated with each file. Requests may be sent to any of the corresponding authors.

Field-specific reporting

Please select the one below that is the best fit for your research. If you are not sure, read the appropriate sections before making your selection.

☒ Life sciences ☐ Behavioural & social sciences ☐ Ecological, evolutionary & environmental sciences

For a reference copy of the document with all sections, see nature.com/documents/nr-reporting-summary-flat.pdf

Life sciences study design

All studies must disclose on these points even when the disclosure is negative.

Sample size	Sample size was approximated and derived from extensive publications within the hematopoiesis field which are based on previous a priori power testing. No statistical methods were used to pre-determine sample sizes but our sample sizes are in agreement with those reported in previous publications 8,19, 43.
Data exclusions	No data points were excluded.
Replication	Experiments were reproduced at least once to confirm the obtained results. For flow cytometric analyses of the bone marrow, experiments were split into groups of 3-4 control and 3-4 experimental sizes and then repeated at least once in identical fashion to allow for adequate sample sizes as well as independent, replication of cumulative results that were separately obtained.
Randomization	Animals were randomly assigned to control or experimental groups.
Blinding	Experiments were performed in blinded or semi-blinded fashion for experiments involving ICM injections. For the latter setting, the investigator performing the injection of sham or experimental biologic/reagent was not blinded while the 2 collaborators harvesting the data were blinded to the groups. Data acquisition during cell sorting of LSKs was also done in blinded fashion (eg WT vs Myd88 KO) by staff scientists at our flow cytometry core along with all other data acquisition for EM and flow cytometry when possible.

Reporting for specific materials, systems and methods

We require information from authors about some types of materials, experimental systems and methods used in many studies. Here, indicate whether each material, system or method listed is relevant to your study. If you are not sure if a list item applies to your research, read the appropriate section before selecting a response.

Materials & experimental systems

n/a	Involved in the study
☐	☒ Antibodies
☒	☐ Eukaryotic cell lines
☒	☐ Palaeontology and archaeology
☐	☒ Animals and other organisms
☒	☐ Human research participants
☒	☐ Clinical data
☒	☐ Dual use research of concern

Methods

n/a	Involved in the study
☒	☐ ChIP-seq
☐	☒ Flow cytometry
☒	☐ MRI-based neuroimaging

Antibodies

Antibodies used	Flow cytometry antibodies: Biotin ABs and Live/Dead (all at 1:100): CD3 (BioLegend, clone 145-2C11, 100304), CD4 (BioLegend, clone GK1.5, 100404), CD8a (BioLegend, clone 53-6.7, 100704), CD49b (BioLegend, clone DX5, 108904), CD90.2 (BioLegend, clone 30-H12, 105304), CD19

(BioLegend, clone 6D5, 115503), B220 (BioLegend, clone RA3-6B2, 103204), NK1.1 (BioLegend, clone PK136, 108704), TER119 (BioLegend, clone TER-119, 116204), CD11b (BioLegend, clone M1/70, 101204), CD11c (BioLegend, clone N418, 117304) and Gr1 (BioLegend, clone RB6-8C5, 108404), LIVE/DEAD Fixable Aqua Dead Cell Stain (Life Technologies),

Fluorescent AB used at 1:100 dilution: ckit-PE-Cy7 (BioLegend, clone 2B8, 105814), Sca1-BV605 (BioLegend, clone D7, 108133) and Streptavidin-APC-Cy7 (BioLegend, 405208), APC Brdu Flow Kit (BD Biosciences, 552598), CD45 (Biologend, clone 30F11, 103147).

Newly incorporated flow cytometry antibodies for revision:
- CMP: same lineage, Sca-1 and c-Kit antibodies described above along with same BrdU kit. CMPs further identified by staining with CD34 (BD, RAM34, 1:100, 553733) and CD16/32 (Biolegend, 93, 1:100, 101337).
- Chimerism Flow: CD45.1 (Biolegend, A20, 1:100, 110716), CD45.2 (Biolegend, 104,1:100, 109832), CD11b (BioLegend, clone M1/70, 1:100 101212), CD115 (Biolegend, AFS98 , 1:100 135517), Ly6G) Biolegend, 1A8, 1:100 127617).
- Leukocyte Panel all at 1:100 unless noted specifically: anti-CD19–PE/Cy7 (6D5, 1:50, BioLegend), anti-CD3–PE (17A2, 1:50 BioLegend), anti-CD45–AF700 (30-F11, BioLegend), anti-Ly6C–BV605 (HK1.4, BioLegend), anti-Ly6G–FITC (1A8, BioLegend), anti-CD11b–APC (M1/70, BioLegend) and anti-CD115–BV421 (AFS98, BioLegend) antibodies

For imaging: CD31 (Biolegend, clone MEC13.3, 25 uL IV, catalog #s: 102516, 102528, 102508), Sca1 (Biolegend, clone D7, 25 uL IV catalog #s: 108146, 108118, 108108), Chicken anti-GFP (Abcam, 1:50, ab13790), Goat anti-chicken AF555 (Thermofisher, 1:200, A-21437)

Validation

All antibodies used for flow cytometry and microscopy were previously validated for the respective application by the vendor. Individual listings of citations (>5 for all listed antibodies) describe the use of these reagents in the imaging or cytometric application in which they were used on each antibody's manufacturer page which can be accessed using the catalog numbers provided above. Additionally, our laboratory has utilized this panel of intravital microscopy and flow cytometry antibodies in recent publications including (Vandoorne, Rohde D et al Circ Res 2018; 123 (4): 415-427) with the only exception being CD31 and Sca1 antibodies which were conjugated with APC/Fire750 fluorophores which were not commercially available until the last year. These antibodies were tested alongside their respective PE and AF647 conjugated counterparts to ensure specific and comparable labeling. Finally identification of LSKs was performed as recently demonstrated by our lab and others in Frodermann, V., Rohde, D., Courties, G. et al. Exercise reduces inflammatory cell production and cardiovascular inflammation via instruction of hematopoietic progenitor cells. Nat Med 25, 1761–1771 (2019).

Animals and other organisms

Policy information about studies involving animals; ARRIVE guidelines recommended for reporting animal research

Laboratory animals

The following mouse strains were used: Wild type C57BL/6J (purchased from Jackson Labs #000664) and Myd88tm1.1Defr (Myd88 Null, Jackson Lab #009088). Male and female mice aged 10-16 weeks were used for all experiments described. Where appropriate, age- and sex-matched mice were used for experiments. As part of the revision, 8 week old B6.SJL-Ptprca Pepcb/BoyJ (CD45.1 Mice, Jackson Lab #002014) were ordered and used as donors for irradiation experiments to serve as the donor BM.

Wild animals

This study did not involve wild animals.

Field-collected samples

This study did not involve field-collected samples.

Ethics oversight

Animal protocols were approved by the Institutional Animal Care and Use Committee (IACUC) at Massachusetts General Hospital. Mice were housed under certified pathogen-free conditions at Massachusetts General Hospital's Center for Comparative Medicine. All experiments were conducted in accordance with IACUC-approved protocols #s 2005N000306, 2019N000203, 2009N000085 and 2007N000148.

Note that full information on the approval of the study protocol must also be provided in the manuscript.

Flow Cytometry

Plots

Confirm that:

☒ The axis labels state the marker and fluorochrome used (e.g. CD4-FITC).

☒ The axis scales are clearly visible. Include numbers along axes only for bottom left plot of group (a 'group' is an analysis of identical markers).

☒ All plots are contour plots with outliers or pseudocolor plots.

☒ A numerical value for number of cells or percentage (with statistics) is provided.

Methodology

Sample preparation

To assess skull and tibia bone marrow hematopoietic cells, mice were anesthetized, sacrificed and perfused with 20 mL PBS to remove blood cells. Tibia and skull were excised, and then meninges were removed from the skull and mechanically homogenized in homogenization buffer (PBS with 5% BSA and 2 mM EDTA). Homogenate was filtered through a 40 µm strainer, centrifuged for 5' at 340g and resuspended in FACS buffer (PBS with 0.5% BSA) for surface antibody staining. Antibody panels used are described above in greater detail in the "Antibody" section. Briefly, cells were first stained with biotin-conjugated anti-mouse antibodies against CD3 (BioLegend, clone 145-2C11), CD4 (BioLegend, clone GK1.5), CD8a (BioLegend, clone 53-6.7), CD49b (BioLegend, clone DX5), CD90.2 (BioLegend, clone 30-H12), CD19 (BioLegend, clone 6D5),

B220 (BioLegend, clone RA3-6B2), NK1.1 (BioLegend, clone PK136), TER119 (BioLegend, clone TER-119), CD11b (BioLegend, clone M1/70), CD11c (BioLegend, clone N418) and Gr1 (BioLegend, clone RB6-8C5 all diluted 1:100), which all served as lineage (Lin) markers, and LIVE/DEAD Fixable Aqua Dead Cell Stain (Life Technologies, 1:100). Staining was done for 30 minutes on ice followed by a wash/spin and resuspension in FACs buffer for secondary staining. LSK identification was performed by staining cells with ckit-PE-Cy7 (BioLegend, clone 2B8), Sca1-BV605 (BioLegend, clone D7) and Streptavidin-APC-Cy7 (BioLegend, 1:100). LSK were identified as Lin- c-kit+ Sca-1+. CMP were identified as Lin-, c-kit+, Sca-1-, CD34+ and CD16/32+. Staining for CMPs was done above as described with the addition of the CD34 and CD16/32 antibodies which were used at 1:100 dilutions.

For leukocyte analysis in marrow, blood and meninges, tissues were processed in 3 separate ways. Blood was lysed in red blood cell lysis and staining done in a similar set up as that for skull marrow LSK staining once cells were in a single-cell suspension. Antibodies which were used are listed above and were all used at 1:100 dilutions. Marrow was processed above as described while meninges were harvested into homogenization buffer (PBS + 5% BSA + 2 mm EDTA), digested in enzymatic mixture (2.5 mg/ml Collagenase D + 0.1 mg/ml DNase I) for 30 minutes with gentle shaking every 10 minutes. Mixture was then filtered and spun down for resuspension in a staining approach similar to blood and marrow. Antibodies used for meningeal leukocyte and chimerism analysis were also used at 1:100 dilutions.

Instrument

Flow cytometry data were acquired on an LSRII flow cytometer (BD Biosciences, San Jose, CA, USA). For cell-sorting, a BD FACs Aria (BD Biosciences) was used.

Software

Flow data was analyzed with FlowJo 10 software (BD Biosciences). Quantitative analysis of flow data and qPCR data was organized on Microsoft Excel and exported onto GraphPad Prism 10 software (GraphPad). Confocal and 2-photon microscopy data was analyzed on FIJI open-source software v2.1. 3-D reconsructions were generated using Volocity software version 6.3 (PerkinElmer). 2-PM image data was analyzed with MATLAB v2020b code to construct z-stacks and Amira v5.3.2 software was used for microCT data analysis.

Cell population abundance

For sorting of LSKs from WT and Myd88 KO mice, purity was confirmed to be greater than 95% during the duration of all mouse samples sorted as per internal FACs Aria quality control metrics provided by the core.

Gating strategy

All cell populations were pregated on viable and single cells. This was accomplished by first gating on all events outside of those known to be debris in FSC-A x SSC-A plot. A two-step singlet selection process followed by plotting FSC-A x FSC-W and gating in the highest density of cells <100 on the FSC-W y-axis. These cells were subsequently subject to singlet selection by plotting SSC-A x SSC-W and selecting all cells under 100 on the SSC-W y-axis. These two cell populations were >95% of all events included in the plot indicating that a single-cell suspension was achieved throughout the majority of the stained single-cell suspension. Live cells were then selected by gating on all single cells that were Live/Dead Aqua-negative (positive cells which are dead cells uptake the L/D stain) which again was greater than 90% of all events included. The next gating step selected Lin- cells by plotting Lin- on the y-axis and kit on the X-axis. LSK identification was finally achieved by taking the Lin- population of cells and separating them by plotting c-Kit on the y-axis and Sca-1 on the x-axis. This allowed us to select Lin-Kit +Sca1+ cells which are the well-established LSK cell population. Where indicated, LSK proliferation was analyzed by gating on LSKs and identifying Brdu+ cells from Brdu- cells by plotting Brdu+ on the y-axis and FSC-W on the x-axis. A representative gating strategy is presented in Figure 7. For CMP analysis, lin- cells were then gated in c-kit+/Sca-1- with CMP identification ultimately performed by finding CD16/32 intermediate/CD34+ cells.

For leukocyte analysis, cells were first analyzed above for single cell and live dead identification. Leukocytes were next identified on CD45+ gating. Cells were further divided into myeloid and lymphoid populations by gating for CD11b+ (myeloid specific) and CD3+/CD19+ (Lymphoid cells). CD11b+ myeloid cells were subdivided into monocytes (CD115+, Ly6g- followed by Ly6C hi and Ly6c Lo status) as well as neutrophils (CD115-, Ly6g+).

For chimerism studies, cells were first analyzed for single cell and live dead identification. Next myeloid cells were identified by gating on all CD11b+ events. These events were then subdivided into either CD45.1+ or CD45.2+ status for % myeloid chimerism. For subset specific chimerism, CD11b+ cells were further gated for identification of monocytes (CD115+, Ly6g-) and neutrophils (CD115-, Ly6g+). Monos and Neutrophils were independently further subdivided into CD45.1/CD45.2 class to determine relative chimerism.

For gating of DiL or DiD LSKs, single cell suspension of skull were stained for live cells. FMO controls for cells lacking DiD or DiL were used to set gates for their respective channels i.e. cells stained with live/dead and DiD were used to set the gate for DiL- cells and vice-versa for DiD. All gating strategies are thoroughly described and shown in extended figures.

☒ Tick this box to confirm that a figure exemplifying the gating strategy is provided in the Supplementary Information.